Supplementary Information

Optimizing the spin qubit performance of lanthanide-based metal−organic frameworks

Xiya Du[a,b,c] and Lei Sun[*b,c,d]

[a]Department of Chemistry, Zhejiang University, Hangzhou, Zhejiang Province 310058, China.

[b]Department of Chemistry, School of Science and Research Center for Industries of the Future, Westlake University, Hangzhou, Zhejiang Province 310030, China.

[c]Institute of Natural Sciences, Westlake Institute for Advanced Study, Hangzhou, Zhejiang Province 310024, China.

[d]Key Laboratory for Quantum Materials, Department of Physics, School of Science, Westlake University, Hangzhou, Zhejiang Province 310030, China

* E-mail: sunlei@westlake.edu.cn

Contents

Materials

All commercially available chemicals were used without further purification. $La(NO_3)_3 \cdot 6H_2O$ (98%) was purchased from Meryer. $Nd(NO_3)_3 \cdot 5H_2O$ (99%) was purchased from Macklin. $Gd(NO_3)_3 \cdot 6H_2O$ (99.9%) and $[N(C_2H_5)_4]Cl$ (98%) were purchased from Aladdin. Chloranilic acid (98%) was purchased from Alfa-Aesar. N,N-dimethylformamide (DMF; AR grade) was purchased from Hushi. H_2O was deionized H_2O from the laboratory.

Synthesis

Ln(CAN) (Ln^{3+} = La^{3+}, Nd^{3+}, Gd^{3+}; CAN^{2-} = chloranilate) were synthesized by solvothermal methods based on literature procedures.[1] 0.114 mmol Ln(NO3)3·mH2O (Ln^{3+} = La^{3+}, Nd^{3+}, Gd^{3+}; m = 5 or 6), 0.227 mmol chloranilic acid, and 1.49 mmol $[N(C_2H_5)_4]Cl$ were weighed by an analytical balance (Mettler-Toledo ME204) and were added into a 20 mL scintillation vial. 10 mL DMF and 0.338 mL H_2O were added to the vial. The reactants were uniformly mixed in the solvent via shaking or ultrasonication. The dark purple-red suspension was kept on a heating plate at 130 ℃ for 16 h. The product was washed several times with DMF and was dried in vacuum on a Schlenk line. $\mathbf{Nd_xLa_{100-x}}$ (x = 0.5, 1, 4, 20) and $\mathbf{Gd_yLa_{100-y}}$ (y = 0.1, 0.5, 1, 20) samples with different doping levels were synthesized with the same procedures by mixing $Ln(NO_3)_3 \cdot mH_2O$ with designated molar ratio as reactants.

Basic characterization

Powder X-ray diffraction (PXRD) patterns were collected at the Bruker D8 Advance diffractometer with Cu Kα radiation (λ = 1.5406 Å) at room temperature. The tube voltage and current were 40 kV and 40 mA, respectively. The diffraction angle (2θ) ranged of 5−50 º was obtained every 0.02 º with a scan speed of 0.1 s/step.

Inductively coupled plasma atomic emission spectroscopy (ICP-AES) was performed on the Thermo Fisher Scientific ICAP PRO XP.

Scanning electron microscopy (SEM) and energy dispersive X-ray spectroscopy

(EDS) were conducted on the Zeiss Gemini 450 SEM with an operating voltage of 3.00 kV and a current of 500 pA.

X-band continuous wave (CW) EPR spectroscopy

X-band (~9.6 GHz) CW EPR experiments were conducted for **Nd_4La_{96}** and Gd_1La_{99} on the CIQTEK EPR100 spectrometer equipped with a 1.8 T bipolar Helmholtz electromagnet, a dielectric resonator, and a liquid-helium-free temperature control system. Samples were vacuum-sealed in background-free quartz tubes (4 mm o.d.) with heights being approximately 1.5 cm. The CW EPR spectra were collected with a microwave power of 0.2 mW, a modulation amplitude of 0.2 mT for **Nd_4La_{96}** (0.1 mT for **Gd_1La_{99}**), and a conversion time of 100 ms. They were fitted using Easyspin 6.0.0 on MATLAB R2024a.[2]

The CW EPR spectrum of **Nd_4La_{96}** was acquired at 8 K. The effective spin Hamiltonian is

$$\hat{H} = \mu_B \boldsymbol{B^T g \hat{S}} + \hat{\boldsymbol{S}}^T \boldsymbol{A \hat{I}} \quad \text{(S1)}$$

where the first term represents the Zeeman splitting of electron spin, and the second term represents the hyperfine interaction between electron spin and Nd nuclear spin.[2] μ_B represents the Bohr magneton, $\boldsymbol{g}$ the g-tensor, $\hat{\boldsymbol{S}}$ the electron spin operator, $\boldsymbol{A}$ the hyperfine coupling tensor, and $\hat{\boldsymbol{I}}$ the nuclear spin operator.

The CW EPR spectrum of Gd_1La_{99} was acquired at 90 K. The effective spin Hamiltonian is

$$\hat{H} = g_{iso}\mu_B \boldsymbol{B^T} \cdot \hat{\boldsymbol{S}} + D\left[\hat{S}_Z^2 - \frac{1}{3}S(S+1)\right] + E\left(\hat{S}_x^2 - \hat{S}_y^2\right) + B_4^0\,\hat{O}_4^0 + B_4^2\,\hat{O}_4^2 \quad \text{(S2)}$$

where the first term is the electron spin Zeeman splitting, the second and third are second-order zero-field splitting, and the last three are fourth-order zero-field splitting ($\hat{O}_4^0, \hat{O}_4^2, \hat{O}_4^4$ are the extended Stevens operators, B_4^0, B_4^2, B_4^4 are the associated coefficients).[3,4] The Stevens operators $\hat{O}_k^q$ (with coefficients B_k^q) are

$$\hat{O}_4^0 = 35\hat{S}_z^4 - [30S(S+1) - 25]\hat{S}_z^2 \quad \text{(S3)}$$

$$\hat{O}_4^2 = \frac{1}{4}[7\hat{S}_z^2 - S(S+1) - 5](\hat{S}_+^2 + \hat{S}_-^2) + \frac{1}{4}(\hat{S}_+^2 + \hat{S}_-^2)[7\hat{S}_z^2 - S(S+1) - 5] \quad \text{(S4)}$$

$$\hat{O}_4^4 = \frac{1}{2}(\hat{S}_+^4 + \hat{S}_-^4) \quad \text{(S5)}$$

X-band pulse EPR spectroscopy

X-band (~9.6 GHz) pulse EPR experiments were conducted for $\mathbf{Nd_xLa_{100-x}}$ (x = 0.5, 1, 4) and $\mathbf{Gd_yLa_{100-y}}$ (y = 0.1, 0.5, 1) on the CIQTEK EPR100 spectrometer equipped with a 1.8 T bipolar Helmholtz electromagnet, a dielectric resonator, and a liquid-helium-free temperature control system. Samples were vacuum-sealed in background-free quartz tubes (4 mm o.d.) with heights being approximately 1.5 cm.

Without further specification, π/2 and π pulses with lengths of 16 ns and 32 ns, respectively, were used. The pulse lengths were optimized by adjusting the microwave attenuation under the guidance of a three-pulse nutation experiment (nutation pulse – t – π/2 – τ – π – τ – echo). To reduce the influence of noise, the threshold for the ends of the echo integrator gate was set about 1/3 height of the echo from the baseline. The shot repetition time (SRT) was set to be longer than five times of the spin relaxation time (T_1) to ensure that all spins have enough time to return to the thermal equilibrium state.

The echo-detected field sweep (EDFS) spectrum was collected with the Hahn echo sequence (π/2 – τ – π – τ – echo) by changing the magnetic field with 4096 data points and 32 shots per point. The experimental temperature was 3.4 K and 3.2 K for $\mathbf{Nd_xLa_{100-x}}$ and $\mathbf{Gd_yLa_{100-y}}$, respectively. For all samples, τ was set as 250 ns. Two-step phase cycling (+x, +x; -x, +x) was used to cancel the background drift and defense pulse. Integration of the echo was plotted against the magnetic field, giving an EDFS spectrum.

The T_1 was measured by employing the picket-fence saturation recovery sequence (π/2 – t1 – π/2 – t1 – π/2 – t1 – π/2 – t1 – π/2 – t1 – π/2 – t1 – π/2 – t1 – π/2 – t – π/2 – τ – π – τ – echo) where with 512 data points at the magnetic field with the maximum EDFS intensity (approximately 264.5 mT for $\mathbf{Nd_xLa_{100-x}}$ and 347.4 mT for $\mathbf{Gd_yLa_{100-y}}$). t1 was fixed at 5000 ns and τ was chosen to ensure relatively strong echo intensity. t started at 400 ns, and its increment was adjusted at each temperature to

make the flat end of the saturation recovery curve account for 1/3 – 1/4 of the entire curve. The shots per point varies with temperature to balance the signal-to-noise ratio and experimental time. In order to cancel the background drift, defense pulse, and other interference echoes, the four-step phase cycling (+x, +x, +x, +x, +x, +x, +x, +x, +x, +x; +x, +x, +x, +x, +x, +x, +x, +x, -x, +x; -x, -x, -x, -x, -x, -x, -x, -x, +x, +x; -x, -x, -x, -x, -x, -x, -x, -x, -x, +x) was conducted. Integration of the echo was plotted against the delay time t, giving the saturation recovery curve. For $\mathbf{Nd_xLa_{100-x}}$, the obtained curves were fitted by a mono-exponential decay function:

$$I = ae^{-\frac{t}{T_1}} + I_0 \quad \text{(S6)}$$

where I is echo intensity, a is a pre-factor, and I_0 is a constant. For $\mathbf{Gd_yLa_{100-y}}$, the obtained curves were fitted by a bi-exponential decay function:

$$I = ae^{-\frac{t}{T_L}} + be^{-\frac{t}{T_S}} + I_0 \quad \text{(S7)}$$

where b is a pre-factor, and T_L and T_S are spin relaxation time constants. Specifically, the longer time constant T_L was considered as T_1, whereas the shorter time constant T_S was attributed to a fast spin relaxation process due to spectral diffusion and/or instantaneous diffusion.[5] The relative ratio between the pre-factors of b/a, reflects the contribution of spectral diffusion and instantaneous diffusion to the spin relaxation. At 80 and 90 K, fitting gives the same T_L and T_S, so the obtained curves were instead fitted by the mono-exponential decay function (Equation S6).

The phase memory time (T_m) was characterized by a two-pulse Hahn echo decay sequence ($\pi/2 - \tau - \pi - \tau -$ echo) with 512 data points at the magnetic field with the maximum EDFS intensity (approximately 264.5 mT for $\mathbf{Nd_xLa_{100-x}}$ and 347.4 mT for $\mathbf{Gd_yLa_{100-y}}$). For all samples, τ was set as 250 ns, and its increment was adjusted at each temperature to make the flat end of the Hahn echo decay curve account for 1/3 – 1/4 of the entire curve. The shots per point varies with temperature to balance the signal-to-noise ratio and experimental time. In order to cancel the background drift and defense pulse, the two-step phase cycling (+x, +x; -x, +x) was employed. Integration of the echo was plotted against 2τ, giving the Hahn echo decay curve.

Without further specification, Hahn echo decay curves were fitted by the mono-exponential decay function:

$$I = ae^{-\frac{2\tau}{T_2}} + I_0 \quad \text{(S8)}$$

Nutation experiments were performed with a three-pulse nutation sequence (nutation pulse – t – π/2 – τ – π – τ – echo) with 1024 data points at the magnetic field with the maximum EDFS intensity (266.0 mT for **$Nd_{0.5}La_{99.5}$** and 348.2 mT for **$Gd_{0.1}La_{99.9}$**). The experimental temperatures were set to 5.2 and 30 K for these two samples, respectively. The delay time t was set as 5000 ns, which is greater than $5T_2$, and τ was fixed at 250 ns. The first length of nutation pulse was 6 ns and the increment was 1 ns. The shots per point was set as 64. In order to cancel the background drift, defense pulse and other interference echoes, the four-step phase cycling (+x, +x, +x; +x, -x, +x; -x, +x, +x; -x, -x, +x) was conducted. Integration of the echo was plotted against the length of nutation pulse, giving the nutation curve that manifests the Rabi oscillation. The time-domain nutation curve was baseline-corrected, apodized by the Hamming window function, zero-filled, and processed by the fast Fourier transform (FFT) with OriginPro 2021. The peaks corresponding to the nutation and the Larmor frequency of ^{1}H were observed in the frequency-domain spectrum. The latter peak is caused by the Hartman–Hahn effect of the precessing ^{1}H nucleus.[6] The former peak is attributed to the Rabi frequency. The nutation experiments were conducted at various microwave attenuations. Rabi frequencies were plotted with $10^{-\frac{A}{20\,dB}}$ (A represents the microwave attenuations in the unit of dB), which reflects the ratio between the magnetic field of the output microwave ($B_{MW\ output}$) and the input microwave ($B_{MW\ input}$).

The combination-peak electron spin echo envelope modulation (CP-ESEEM) vs. τ experiment was conducted by the four-pulse sequence (π/2 – τ – π/2 – t – π – t – π/2 – τ – echo). The delay time τ started at 80 ns and was incremented by 4 ns per step till 320 ns. For each τ, t started at 400 ns and was incremented by 8 ns with 512 data points. This experiment was carried out with 128 shots per point and at the magnetic

field with the maximum EDFS intensity (265.6 mT for **$Nd_{0.5}La_{99.5}$** and 347.6 mT for **$Gd_{0.1}La_{99.9}$**). The experimental temperatures were set to 5.2 and 9 K for these two samples, respectively. In order to cancel the background drift, defense pulse and other interference echoes, the eight-step phase cycling (+x, +x, +x, +x; -x, +x, +x, +x; +x, -x, +x, +x; -x, -x, +x, +x; +x, +x, +x, -x; -x, +x, +x, -x; +x, -x, +x, -x; -x, -x, +x, -x) was conducted. For each τ, integration of the echo was plotted against t, giving a time-domain CP-ESEEM spectrum. This spectrum was baseline-corrected, apodized by the Hamming window function, zero-filled, and processed by the fast Fourier transform (FFT) with the EPR-ProCt. The frequency-domain CP-ESEEM spectrum was plotted against τ, giving a two-dimensional CP-ESEEM vs τ spectrum.

Crystal structures

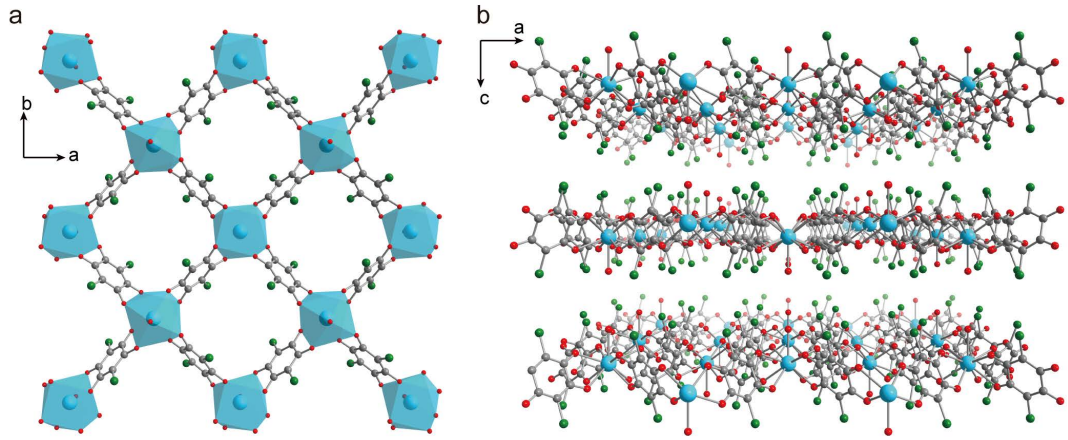

Figure S1. Portions of crystal structure of La(CAN) viewed along the crystallographic (a) *c* axis and (b) *b* axis. Gray, red, green, and cyan spheres represent carbon, oxygen, chlorine, and lanthanum atoms, respectively. Hydrogen atoms and $N(C_2H_5)^+$ cations are omitted for clarity.

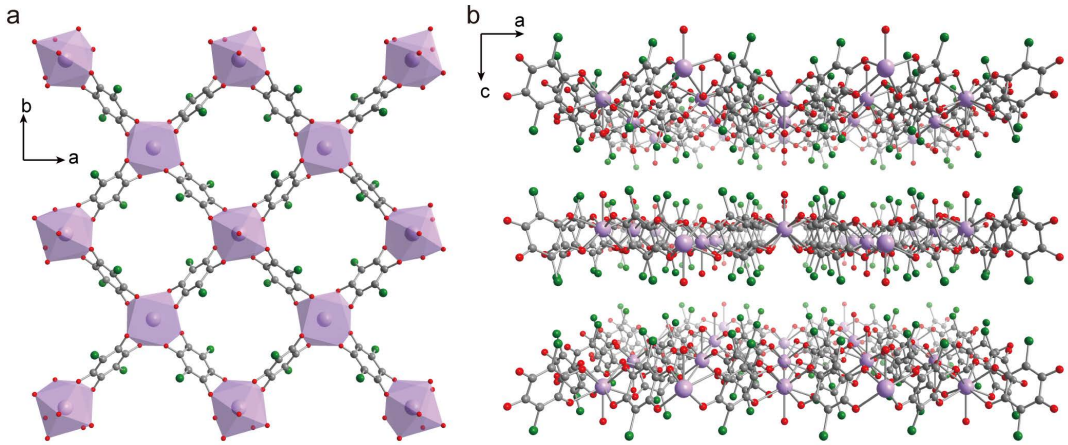

Figure S2. Portions of crystal structure of Nd(CAN) viewed along the crystallographic (a) *c* axis and (b) *b* axis. Gray, red, green, and purple spheres represent carbon, oxygen, chlorine, and neodymium atoms, respectively. Hydrogen atoms and $N(C_2H_5)^+$ cations are omitted for clarity.

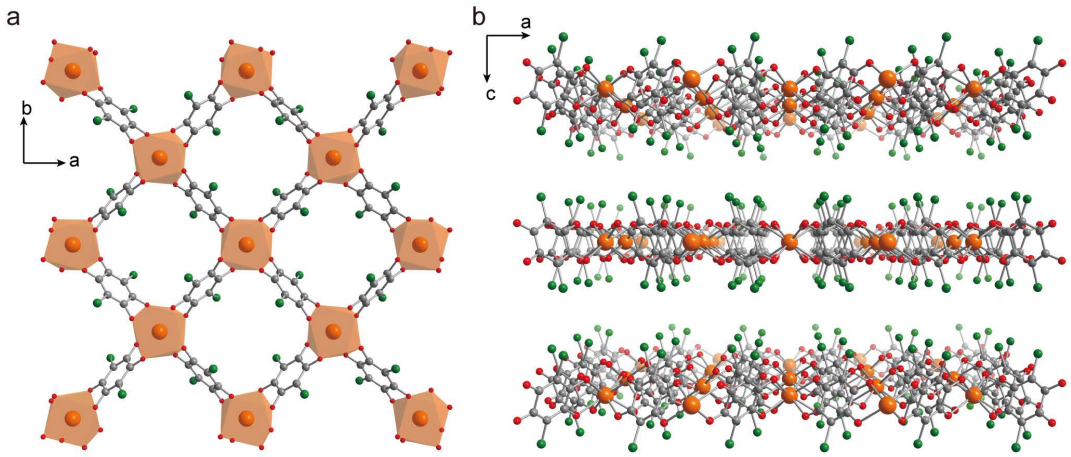

Figure S3. Portions of crystal structure of Gd(CAN) viewed along the crystallographic (a) *c* axis and (b) *b* axis. Gray, red, green, and orange spheres represent carbon, oxygen, chlorine, and gadolinium atoms, respectively. Hydrogen atoms and $N(C_2H_5)^+$ cations are omitted for clarity.

Results of basic characterization

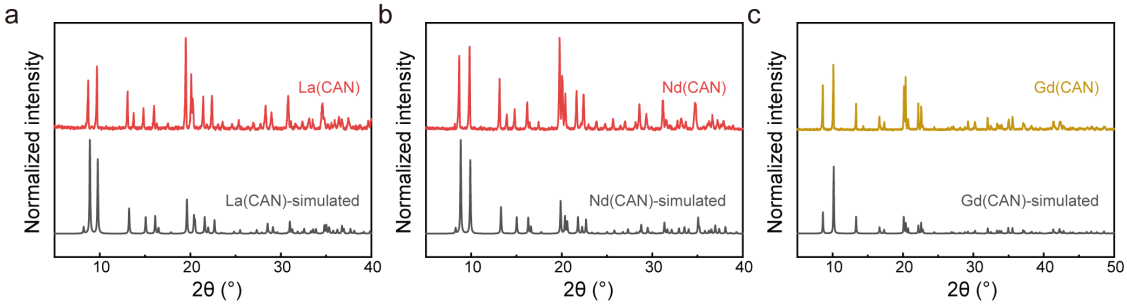

Figure S4. Experimental and simulated PXRD patterns of (a) La(CAN), (b) Nd(CAN), and (c) Gd(CAN).

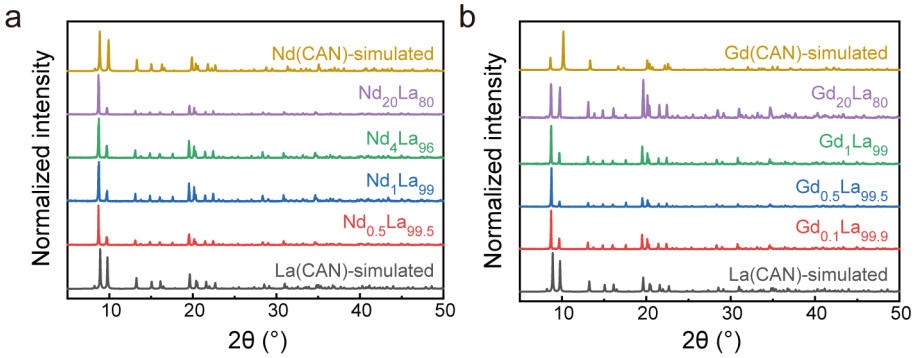

Figure S5. Experimental and simulated PXRD patterns of (a) $\mathbf{Nd_xLa_{100-x}}$ (x = 0.5, 1, 4, 20) and (b) $\mathbf{Gd_yLa_{100-y}}$ (y = 0.1, 0.5, 1, 20).

Table S1. The results of ICP-AES.

Samples	**Contents (%) of Nd in metals**	
	Theoretical value	Experimental value
$Nd_{0.5}La_{99.5}$	0.5	0.50
$Nd_{1}La_{99}$	1.0	0.95
$Nd_{4}La_{96}$	4.0	4.07
$Nd_{20}La_{80}$	20.0	18.9
Samples	**Contents (%) of Gd in metals**	
	Theoretical value	Experimental value
$Gd_{0.1}La_{99.9}$	0.1	0.12
$Gd_{0.5}La_{99.5}$	0.5	0.51
$Gd_{1}La_{99}$	1.0	1.05
$Gd_{20}La_{80}$	20.0	19.61

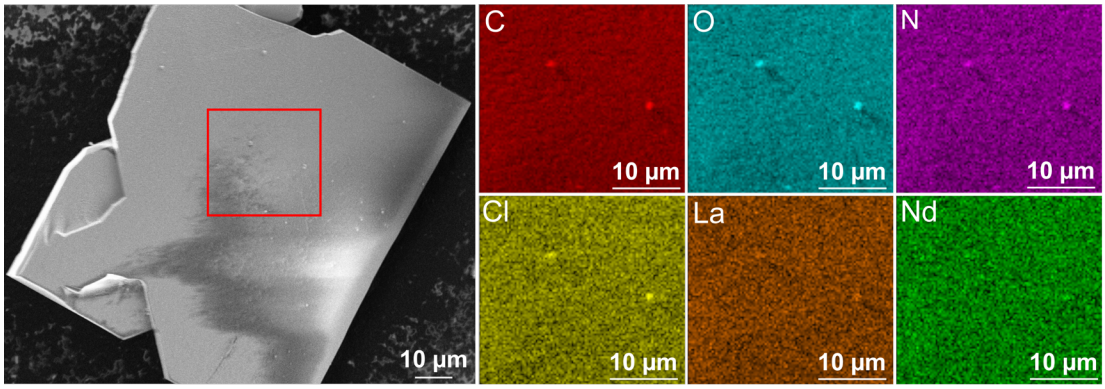

Figure S6. SEM image of **$Nd_{20}La_{80}$** and corresponding EDS mapping in the red box.

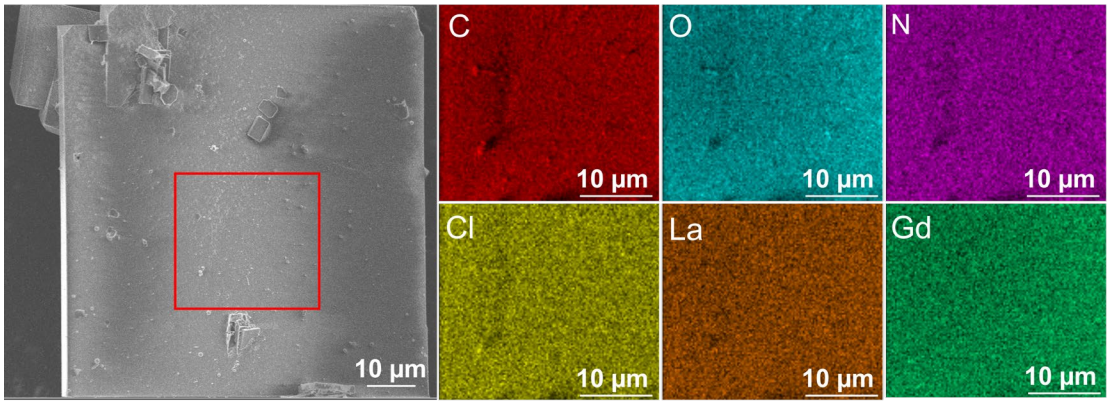

Figure S7. SEM image of **$Gd_{20}La_{80}$** and corresponding EDS mapping in the red box.

Background signals of the microwave resonator

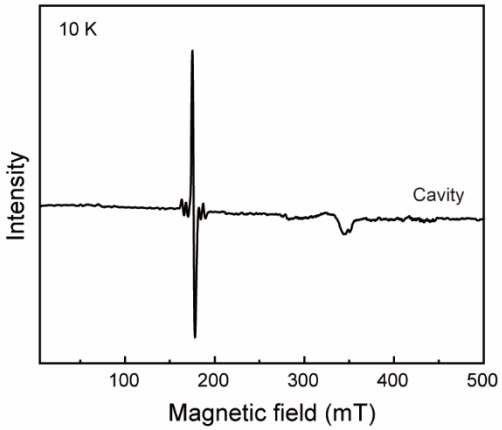

Figure S8. CW EPR spectrum of the microwave resonator collected at 10 K.

Pulse sequences

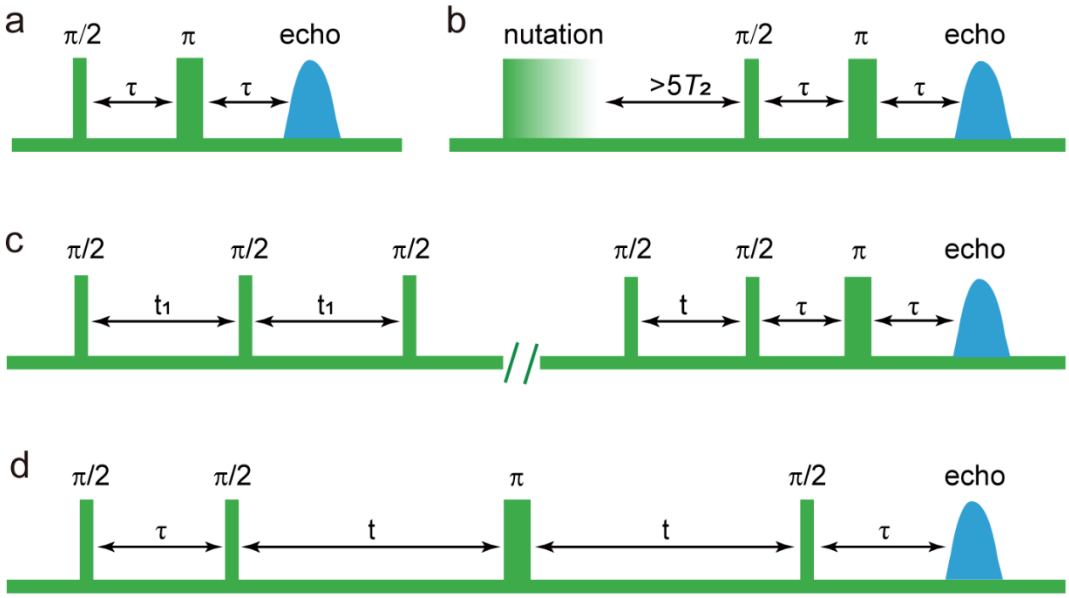

Figure S9. (a) Hahn echo sequence for EDFS and T_2 measurements. (b) Three-pulse nutation sequence. (c) Picket-fence saturation recovery sequence for T_1 measurements. (d) Four-pulse sequence for CP-ESEEM vs. τ experiments.

EDFS spectra

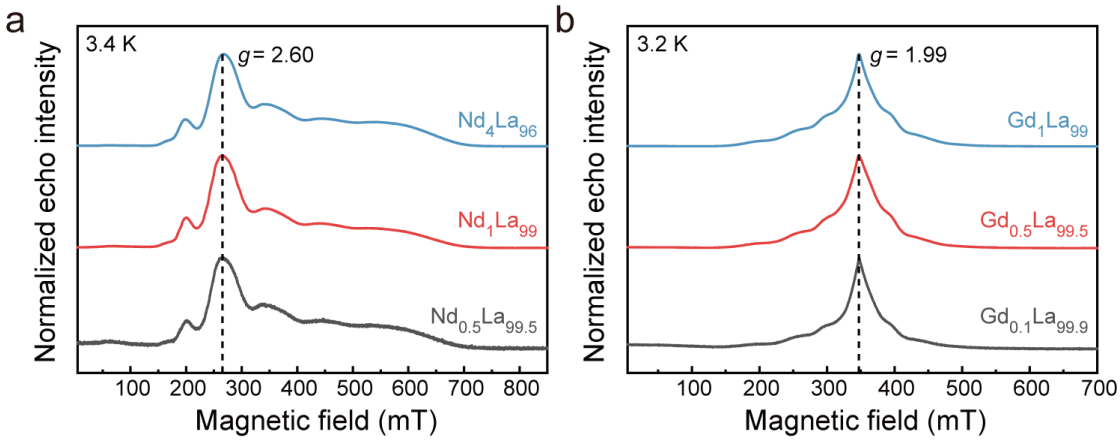

Figure S10. EDFS spectra of (a) $\mathbf{Nd_xLa_{100-x}}$ collected at 3.4 K and (b) $\mathbf{Gd_yLa_{100-y}}$ collected at 3.2 K.

Rabi oscillations

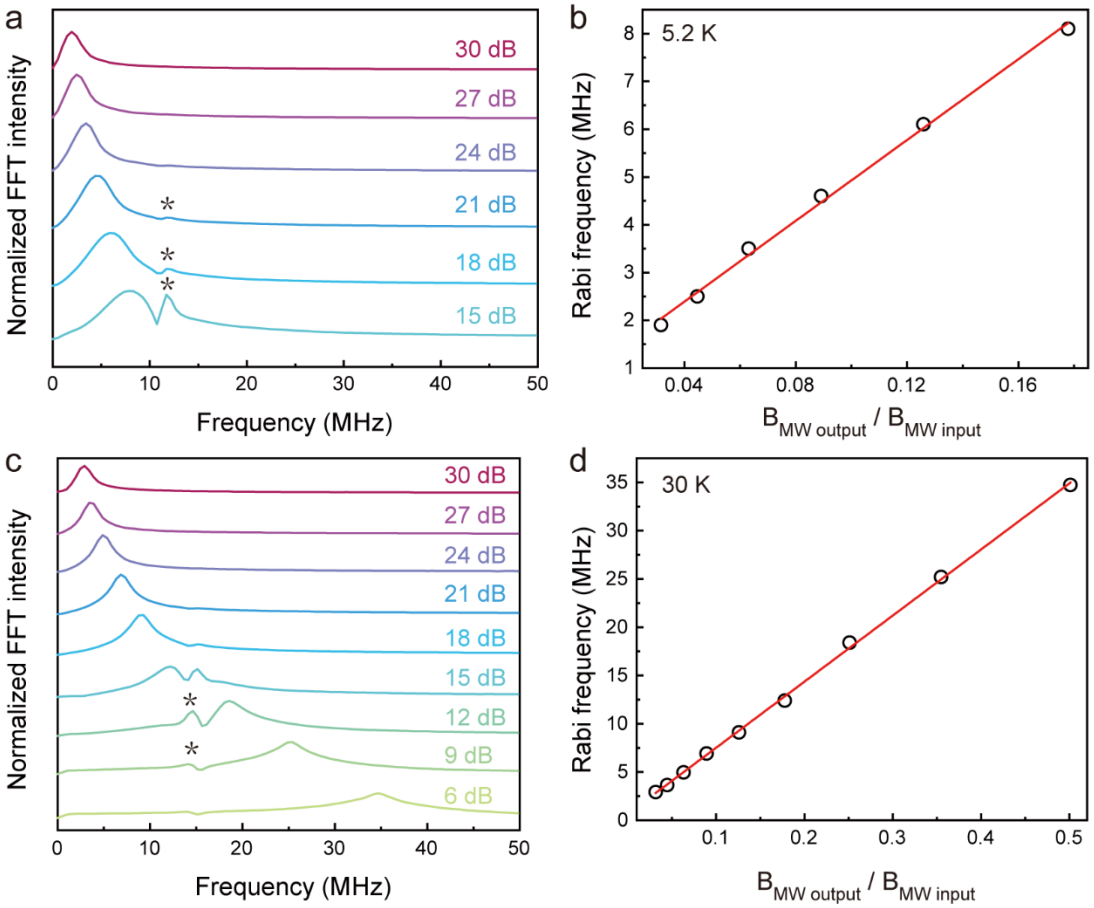

Figure S11. Frequency-domain nutation curves for (a) **$Nd_{0.5}La_{99.5}$** and (c) **$Gd_{0.1}La_{99.9}$**. Peaks marked by asterisks originate from the Hartman-Hahn effect of the precessing ^{1}H nucleus.[6] The relationship of Rabi frequency and ratio between the magnetic field of the output and input microwave for (b) **$Nd_{0.5}La_{99.5}$** and (d) **$Gd_{0.1}La_{99.9}$**. Red lines are linear fits to the data.

Spin relaxation

Note S1. Simulation of Raman relaxation

The Raman relaxation of **Nd_xLa_{100-x}** can be described by the follow equation:

$$\frac{1}{T_1} = A_{Raman}(\frac{T}{T_D})^7 \int_0^{T_D/T} x^6 \frac{e^x}{(e^x-1)^2} dx \quad \text{(S9)}$$

where A_{Raman} represents the pre-factor, T the experimental temperature, T_D the Debye temperature. We simulated the temperature dependence of $1/T_1$ using Equation S9 with T_D = 10 K, 20 K, 40 K, 60 K, 80 K, 100 K and 150 K in the temperature range of 3.2 − 8.0 K. A_{Raman} was chosen to match the simulation curve with the experimental data. As shown in Fig. S15b−d, the Equation S9 can well simulate the experimental results when T_D > 80 K. Indeed, if T_D = 80 K, the integral in Equation S9 changes from 732.5 at T = 3.2 K to 638.8 at T = 8.0 K — it decreases by 12.79% while T^7 increases by 609 times (Fig. S15a). Further improving T_D would saturate the integral even for T = 8.0 K (the integral saturates when T_D/T > 15; see Fig. S15a). Thus, the integral can be approximated as a constant in the temperature range of 3.2 – 8.0 K when T_D > 80 K, giving rise to $1/T_1 \propto T^7$. Due to this temperature dependence of Raman relaxation rate, we can only obtain the lower limit of T_D for **Nd_xLa_{100-x}**, which is 80 K.

Note S2. Cross relaxation of Nd_xLa_{100-x}

The cross relaxation describes the flip-flop between the electron spin of interest and another neighboring electron spin that has similar Larmor frequency. This is an energy-conserving process where one electron spin undergoes $|m\rangle \rightarrow |m+1\rangle$ transition and the other undergoes $|m'+1\rangle \rightarrow |m'\rangle$ transition (m and m' represent spin quantum numbers). The flip-flop rate scales with the dipolar coupling between these two electron spins as well as their Boltzmann population.[7] The transition matrices are

$$W_+ = |< m+1, m' \mid S_1^+ S_2^- \mid m, m'+1 >|^2 = (S-m)(S+m+1)(S-m')(S+m'+1) \quad \text{(S10)}$$

$$W_- = |< m, m'+1 \mid S_1^- S_2^+ \mid m+1, m' >|^2 = (S-m)(S+m+1)(S-m')(S+m'+1) \quad \text{(S11)}$$

where S_1^+ represents the raising operator for the first spin, and S_2^- the lowering operator for the second spin.

Only $m = \pm 1/2$ states of Nd^{3+} are populated in the experimental temperature range (3.2 K − 8.0 K) due to the large zero-field splitting. Consider the flip-flop event between "A" Nd^{3+} (the electron spin of interest) and "B" Nd^{3+} (the neighboring electron spin). For transition matrices, $S = 3/2$ and $m = m' = -1/2$, so $W_+ = W_- = 16$. The rate of "A" Nd^{3+} undergoing $|-1/2\rangle \rightarrow |1/2\rangle$ transition is

$$R_+ = \omega_{dd}(\bar{r}) W_+ n_{A,-1/2} n_{B,1/2} \quad \text{(S12)}$$

where $\omega_{dd}(\bar{r})$ represents the strength of dipolar coupling (in the unit of Hz) between the two electron spins whose average distance is $\bar{r}$, $n_{A,-1/2}$ the Boltzmann population of "A" Nd^{3+} at $|-1/2\rangle$ state, $n_{B,1/2}$ the Boltzmann population of "B" Nd^{3+} at $|1/2\rangle$ state. Similarly, the rate of "A" Nd^{3+} undergoing $|1/2\rangle \rightarrow |-1/2\rangle$ transition is

$$R_- = \omega_{dd}(\bar{r}) W_- n_{A,1/2} n_{B,-1/2} \quad \text{(S13)}$$

The cross relaxation rate of Nd^{3+} describes the total rate of $|1/2\rangle \rightarrow |-1/2\rangle$ relaxation, so it equates the difference between R_- and R_+:

$$\frac{1}{T_1} = A(R_- - R_+) = 16A\omega_{dd}(\bar{r})\left[n_{A,1/2}n_{B,-1/2} - n_{A,-1/2}n_{B,1/2}\right] \quad \text{(S14)}$$

where A is a pre-factor.

We performed picket-fence saturation recovery experiment to acquire the T_1 of **Nd$_x$La$_{100-x}$**. Thus, right after the exertion of the picket-fence saturation pulses, both $m = \pm 1/2$ states of "A" Nd^{3+} are equally populated, i.e. $n_{A,-1/2} = n_{A,1/2} = 0.5$. Therefore, Equation S14 can be re-written as

$$\frac{1}{T_1} = 8A\omega_{dd}(\bar{r})\left[n_{B,-1/2} - n_{B,1/2}\right] = A_{cross}\frac{1-\exp(-h\nu/k_BT)}{1+\exp(-h\nu/k_BT)} \quad \text{(S15)}$$

where $A_{cross} = 8A\omega_{dd}(\bar{r})$, h represents the Planck constant, ν the Larmor frequency (~9.6 GHz), k_B the Boltzmann constant, and T the temperature. As shown in Fig. 4c, the cross relaxation rate decreases with rising temperature in the experimental temperature range. As $\omega_{dd}(\bar{r})$ scales with the spin concentration, the cross relaxation is negligible for **Nd$_{0.5}$La$_{99.5}$** and **Nd$_1$La$_{99}$**, and it becomes salient for **Nd$_4$La$_{96}$**.

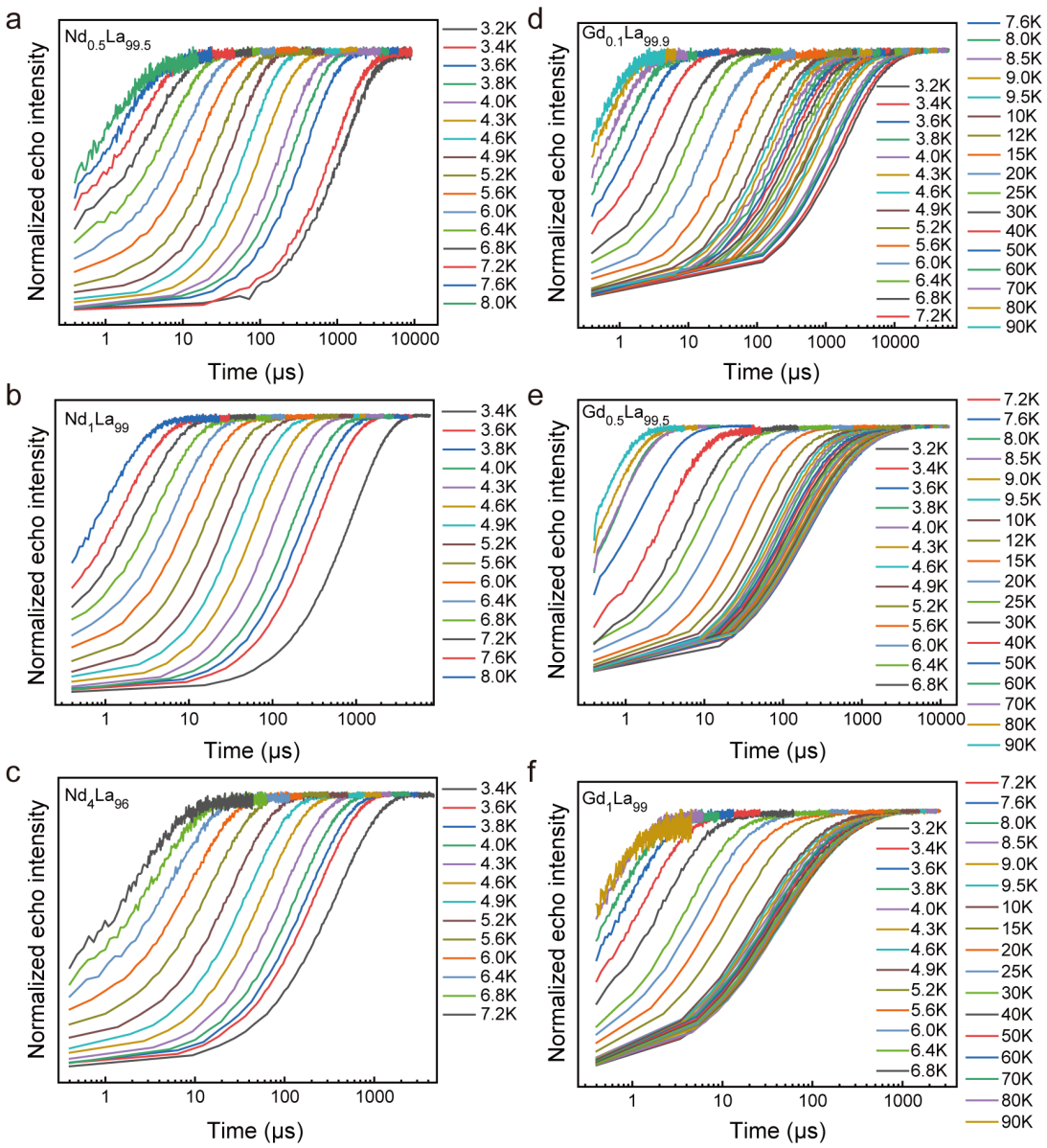

Figure S12. Normalized saturation recovery curves of (a) **$Nd_{0.5}La_{99.5}$**, (b) **Nd_1La_{99}**, and (c) **Nd_4La_{96}** collected at various temperatures from 3.2 K to 8.0 K. Normalized saturation recovery curves of (d) **$Gd_{0.1}La_{99.9}$**, (e) **$Gd_{0.5}La_{99.5}$**, and (f) **Gd_1La_{99}** collected at various temperatures from 3.2 K to 90 K.

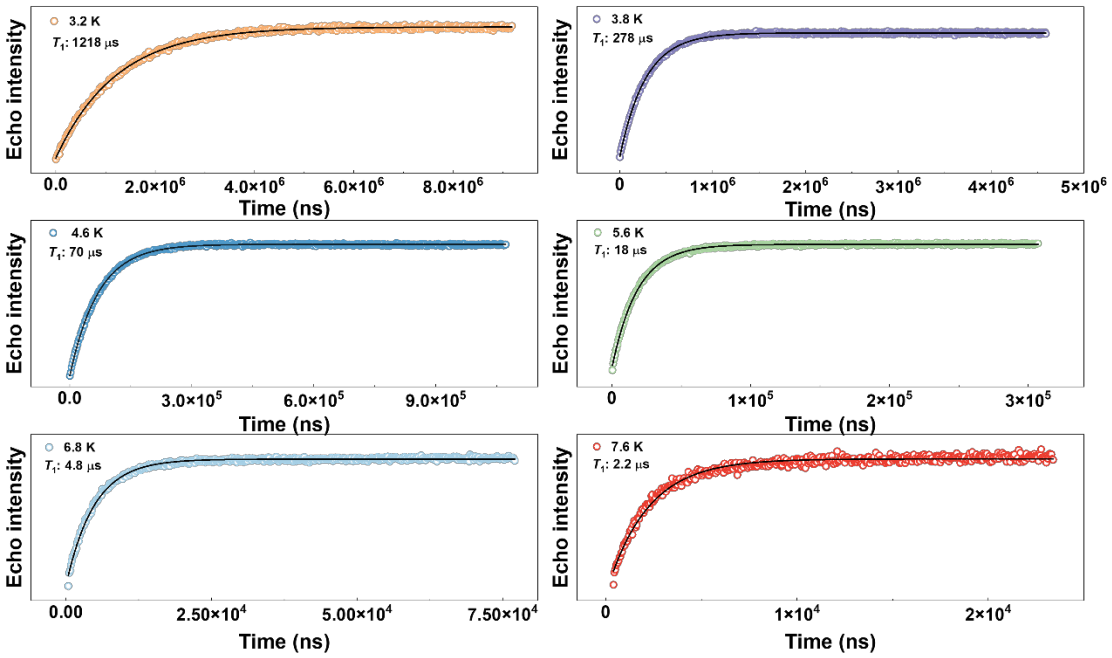

Figure S13. Saturation recovery curves of $Nd_{0.5}La_{99.5}$ fitted by a mono-exponential decay function (Equation S6) at 3.2 K, 3.8 K, 4.6 K, 5.6 K, 6.8 K, and 7.6 K. Black lines are fitting curves.

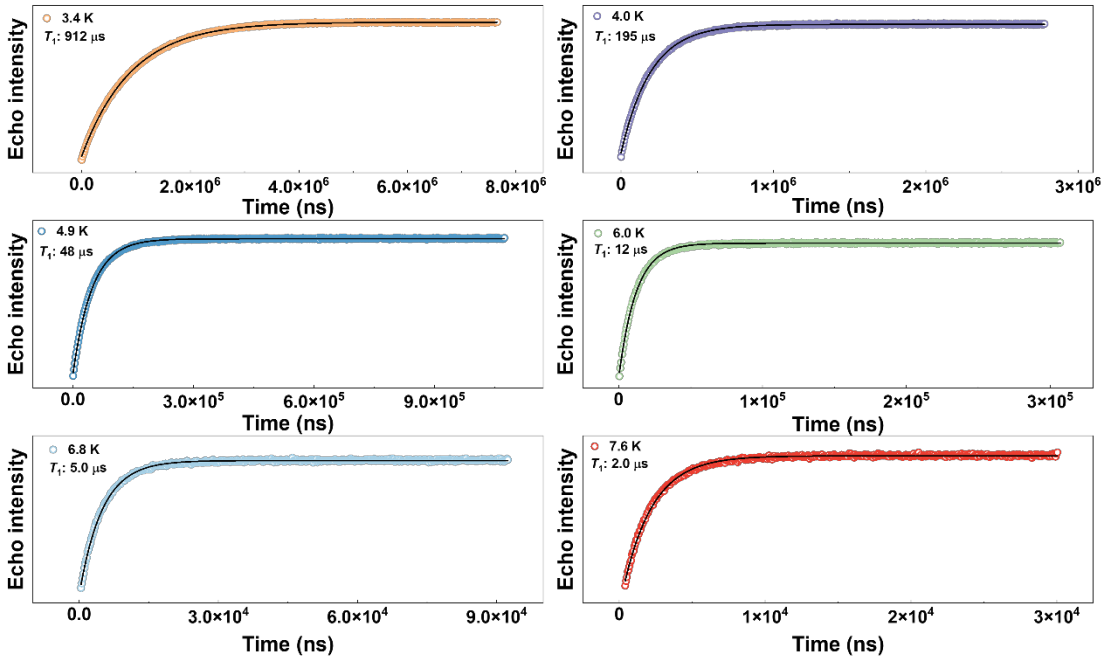

Figure S14. Saturation recovery curves of Nd_1La_{99} fitted by a mono-exponential decay function (Equation S6) at 3.4 K, 4.0 K, 4.9 K, 6.0 K, 6.8 K, and 7.6 K. Black lines are fitting curves.

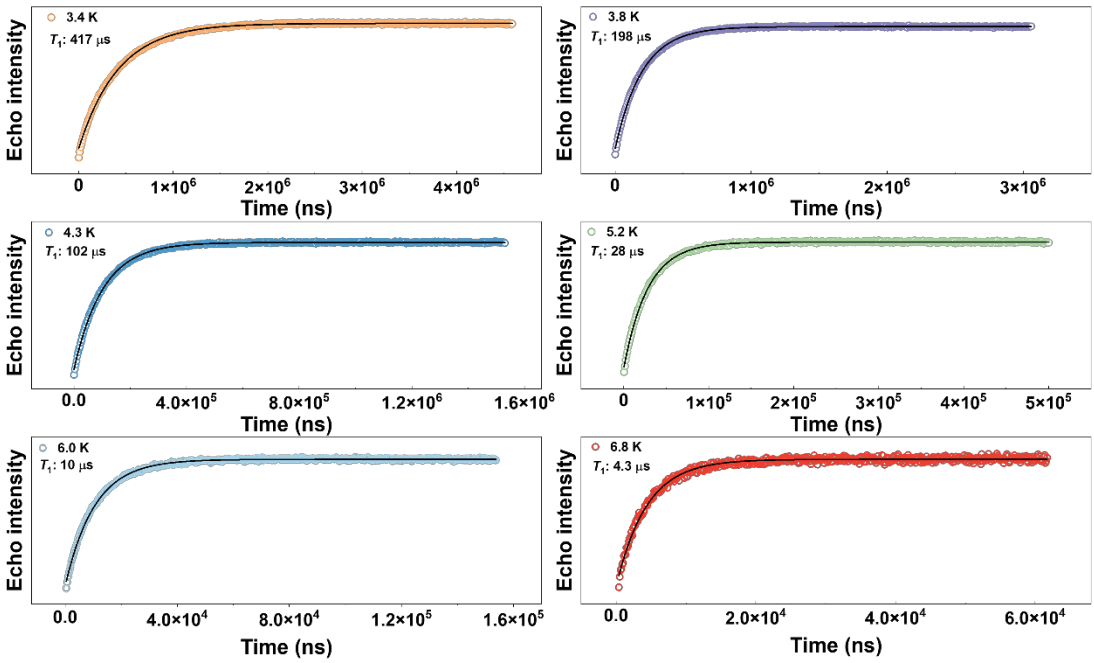

Figure S15. Saturation recovery curves of **Nd_4La_{96}** fitted by a mono-exponential decay function (Equation S6) at 3.4 K, 3.8 K, 4.3 K, 5.2 K, 6.0 K, and 6.8 K. Black lines are fitting curves.

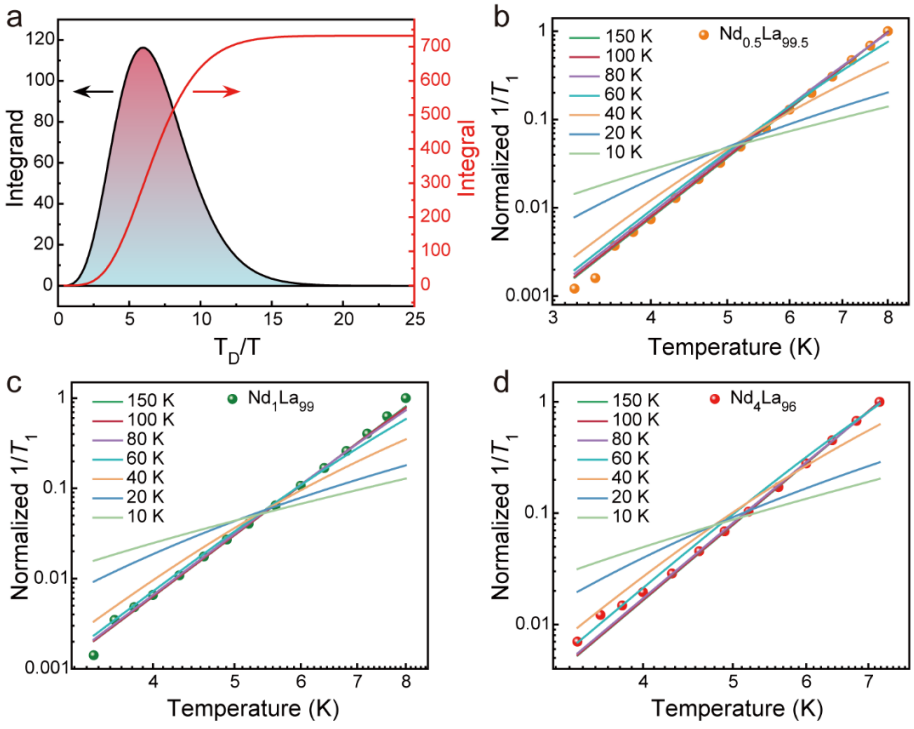

Figure S16. (a) Temperature dependence of integrand and integral in Equation S9. (b–d) Normalized $1/T_1$ vs T data and simulations using Equation S9 with various Debye temperatures for (b) **$Nd_{0.5}La_{99.5}$**, (c) **Nd_1La_{99}**, and (d) **Nd_4La_{96}**.

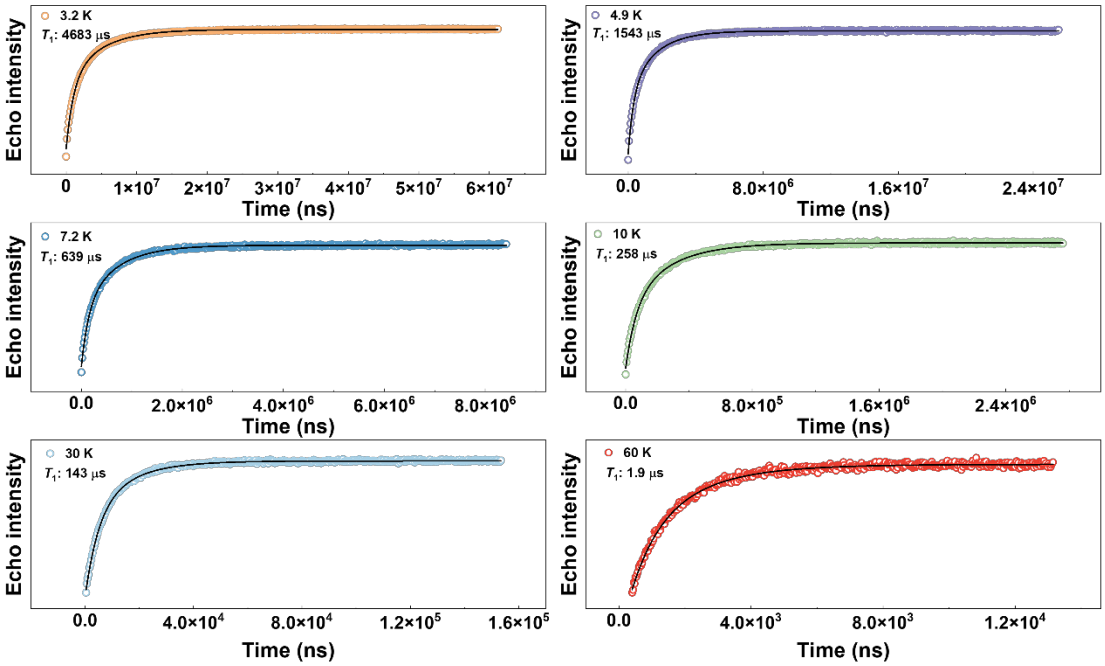

Figure S17. Saturation recovery curves of **$Gd_{0.1}La_{99.9}$** fitted by a bi-exponential decay function (Equation S7) at 3.2 K, 4.9 K, 7.2 K, 10 K, 30 K, and 60 K. Black lines are fitting curves.

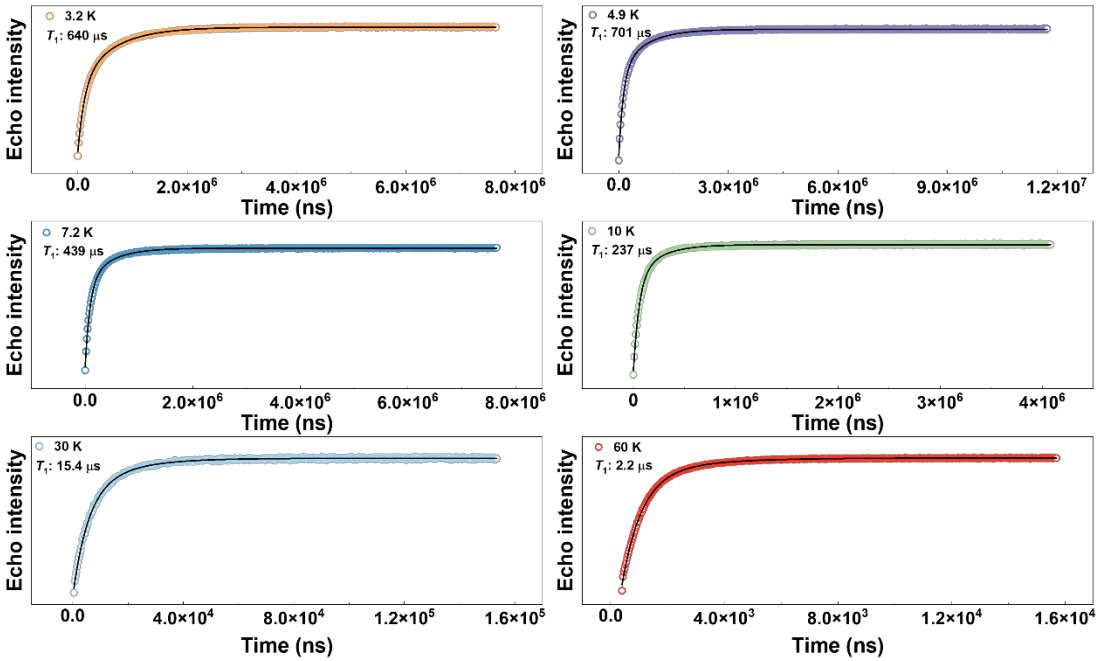

Figure S18. Saturation recovery curves of **$Gd_{0.5}La_{99.5}$** fitted by a bi-exponential decay function (Equation S7) at 3.2 K, 4.9 K, 7.2 K, 10 K, 30 K, and 60 K. Black lines are fitting curves.

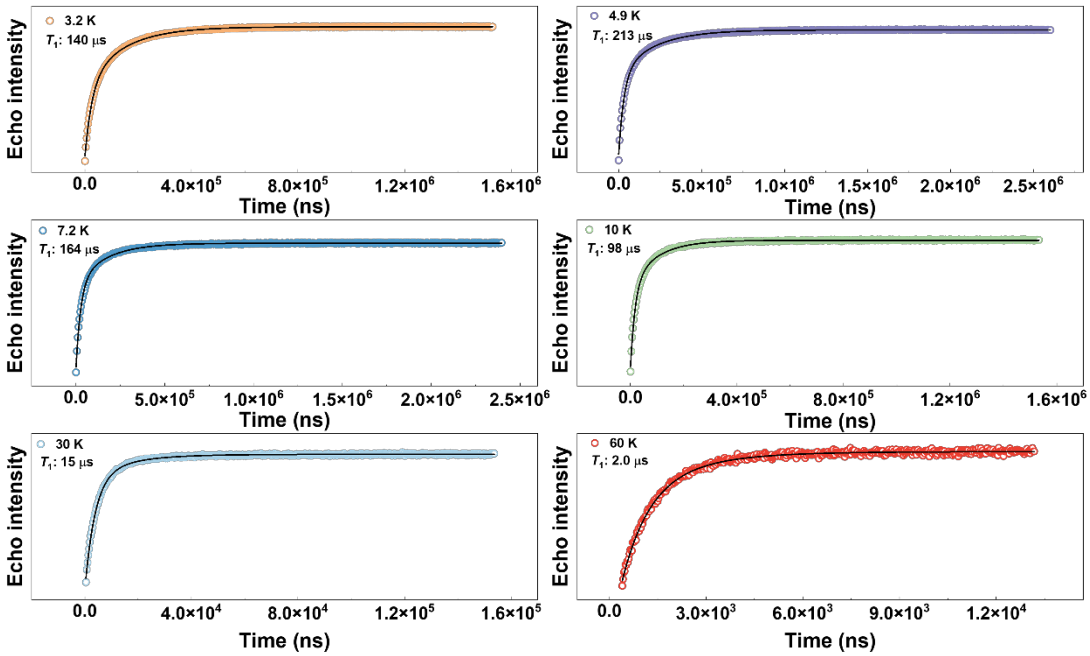

Figure S19. Saturation recovery curves of **Gd_1La_{99}** fitted by a bi-exponential decay function (Equation S7) at 3.2 K, 4.9 K, 7.2 K, 10 K, 30 K, and 60 K. Black lines are fitting curves.

Spin decoherence

Note S3. Decoherence caused by electron spin flip-flop

In addition to the cross relaxation discussed in Note S2, the mutual flip-flop between two adjacent electron spins, which have similar Larmor frequencies, also causes decoherence. When the electron spin of interest is involved, spin flip-flop reverses the spin state and destroys the coherence directly. When two electron spins that are close to the electron spin of interest undergo flip-flop, the local magnetic field changes, which induces decoherence indirectly.[8] As discussed in Note S2, the rate of flip-flop is related to dipolar coupling between two electron spins as well as the thermal population in each spin sublevel. Thus, it scales with spin concentration and may be temperature-dependent.

We applied electron spin flip-flop models derived by Takahashi et al.[7] and Wilson et al.[8] to understand the decoherence of $\mathbf{Nd_xLa_{100-x}}$ and $\mathbf{Gd_yLa_{100-y}}$. Different from the situation of T_1 measurements (Note S2), T_m was acquired by the Hahn echo decay pulse sequence, so all Nd^{3+} electron spins obey the Boltzmann distribution. Based on Takahashi's model[7] and applying Equation S12 and S13, the decoherence rate of $\mathbf{Nd_xLa_{100-x}}$ caused by spin flip-flop can be described with the following equation:

$$\frac{1}{T_{m,flip-flop}} = A(R_+ + R_-) = A\omega_{dd}(\bar{r})(W_+ + W_-)n_{-1/2}n_{1/2} = A\omega_{dd}(\bar{r})W_{Nd} \quad \text{(S16)}$$

where W_{Nd} represents the electron spin flip-flop probability for Nd^{3+}. Applying the Boltzmann distribution and Equation S10 and S11, W_{Nd} can be expressed as

$$W_{Nd} = 32\frac{\exp\left(-\frac{h\upsilon}{k_B T}\right)}{\left[1+\exp\left(-\frac{h\upsilon}{k_B T}\right)\right]^2} \quad \text{(S17)}$$

As shown in Fig. S29a, W_{Nd} is essentially temperature-independent in the experimental temperature range (3.2 K − 8 K). Therefore, the decoherence rate induced by the electron spin flip-flop can be considered as a temperature-independent constant for Nd^{3+}.

For $\mathbf{Gd_yLa_{100-y}}$, the ground spin state of Gd^{3+} is S = 7/2 and the zero-field

splitting is small. Thus, the flip-flop can occur between any two Zeeman levels given energy conservation. Based on Wilson's model,[8] the decoherence rate caused by spin flip-flop can be described with the following equation:

$$\frac{1}{T_{m,flip-flop}} = A\omega_{dd}(\bar{r})W_{Gd} = A\omega_{dd}(\bar{r})\sum_{m=-S}^{S-1}\sum_{m'=-S+1}^{S}W_{m,m'}n_m n_{m'} \quad \text{(S18)}$$

where $W_{m,m'} = W_+ + W_-$ (Equation S10 and S11), W_{Gd} represents the electron spin flip-flop probability for Gd^{3+}, and n_m and $n_{m'}$ represent the Boltzmann population of $|m\rangle$ and $|m'\rangle$ states, respectively. The energy of each Zeeman level can be calculated based on the g-factor and zero-field splitting parameters extracted from the CW EPR experiment (Fig. 2b).

As shown in Fig. S29b, as temperature increases from 0 K, W_{Gd} first increases rapidly and reaches the peak value at approximately 2.6 K. Nonetheless, in the experimental temperature range, W_{Gd} decreases slowly with rising temperature — it declines by 6% from 3.2 K to 90 K. Therefore, the decoherence rate induced by the electron spin flip-flop can be approximated as a temperature-independent constant for Gd^{3+}.

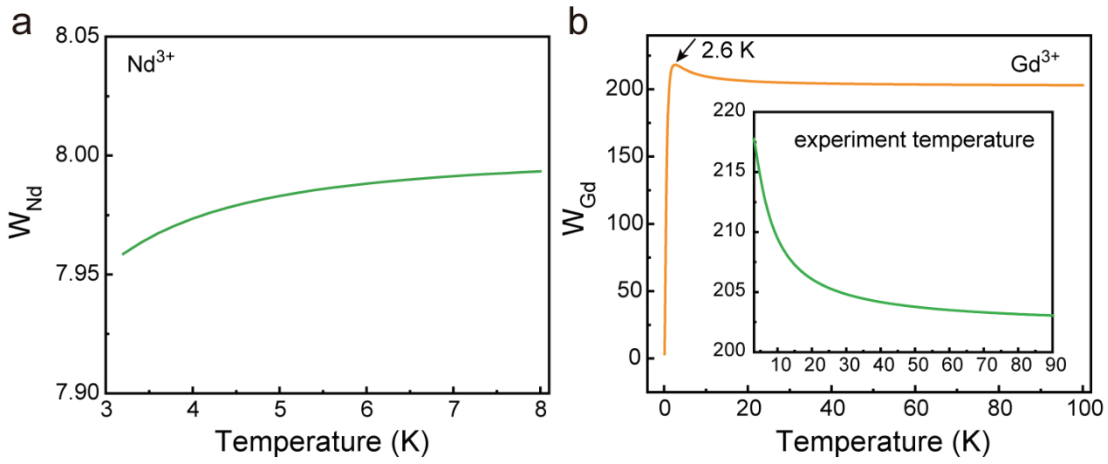

Figure S20. Temperature dependence of electron spin flip-flop probability for (a) **Nd_xLa_{100-x}** and (b) **Gd_yLa_{100-y}**.

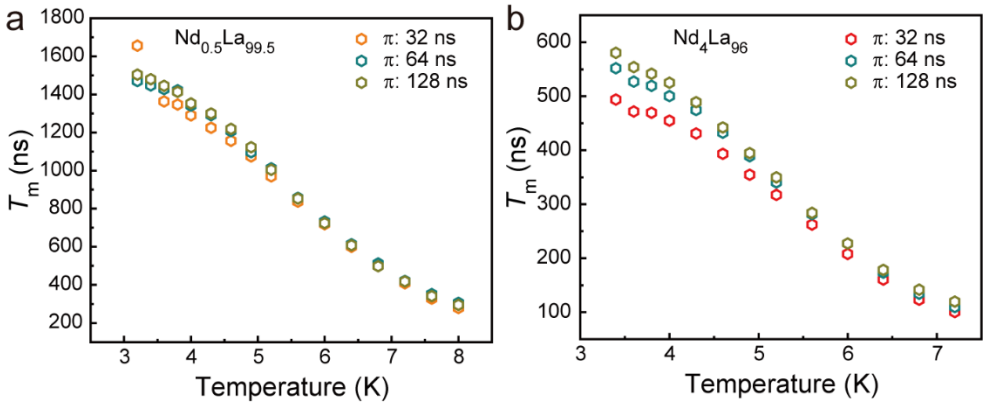

Figure S21. Variable-temperature T_m of (a) **$Nd_{0.5}La_{99.5}$** and (b) **Nd_4La_{96}** using various π pulse lengths.

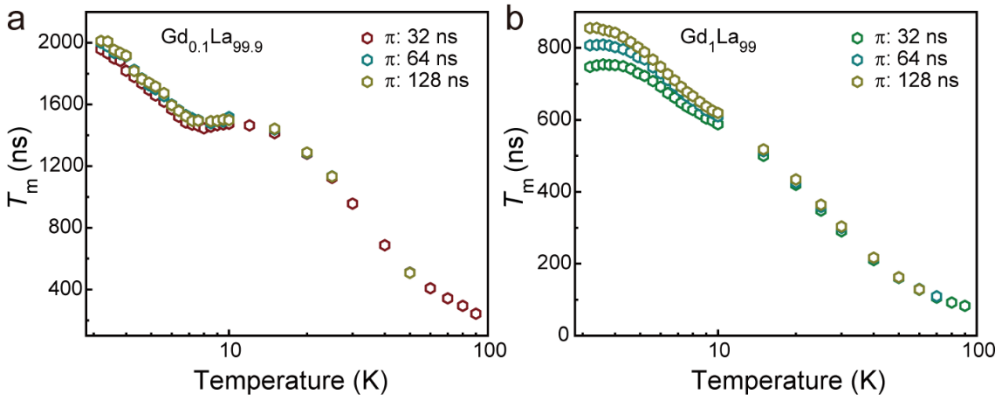

Figure S22. Variable-temperature T_m of (a) **$Gd_{0.1}La_{99.9}$** and (b) **Gd_1La_{99}** using various π pulse lengths.

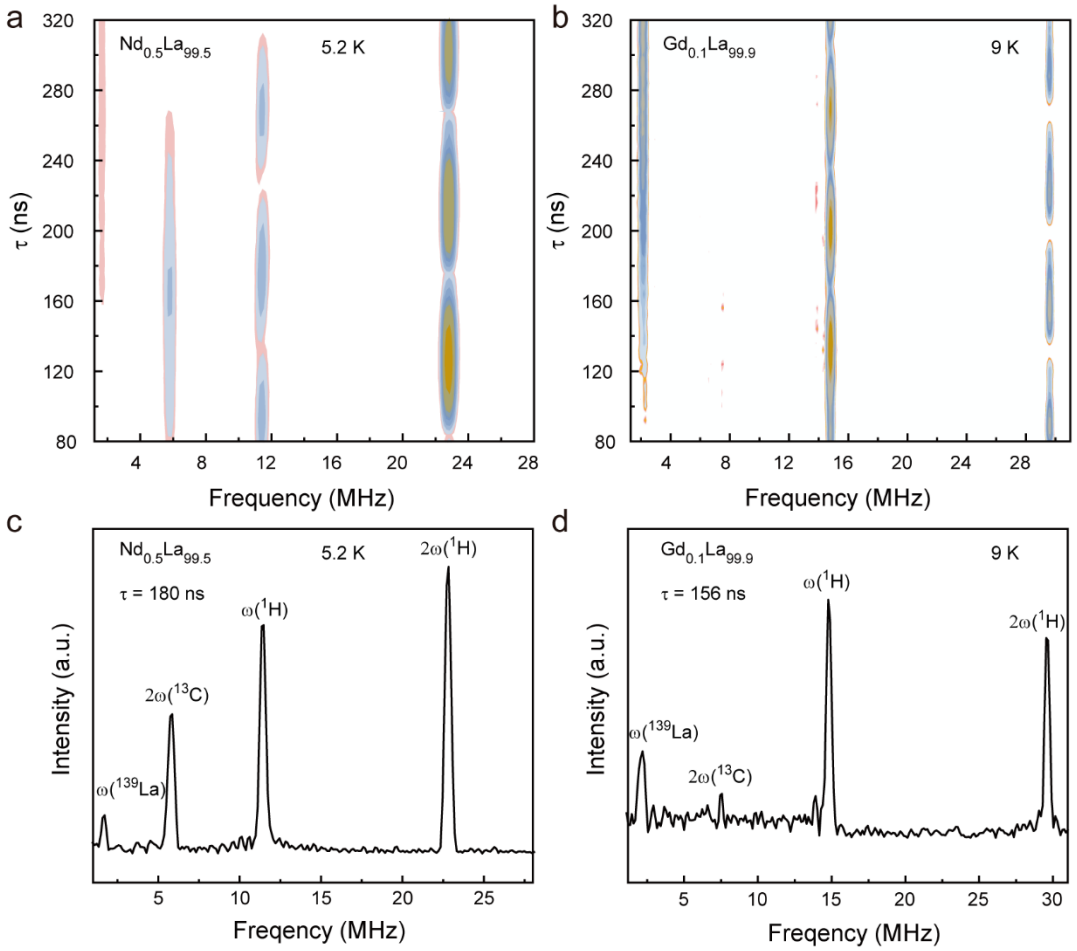

Figure S23. Two-dimensional CP-ESEEM vs. τ spectra of (a) **$Nd_{0.5}La_{99.5}$** and (b) **$Gd_{0.1}La_{99.9}$**. Frequency-domain CP-ESEEM spectra of (c) **$Nd_{0.5}La_{99.5}$** and (d) **$Gd_{0.1}La_{99.9}$**.

Note S4. Influence of the Shot Repetition Time (SRT) on T_m measurements

In the Hahn echo decay experiments, if the SRT is not sufficiently long, it may lead to underestimation of the T_m.[9] We checked the impact of SRT on the T_m characterization exemplified by **Nd$_1$La$_{99}$** and **Gd$_{0.5}$La$_{99.5}$**. Various SRT, Shots Per Point (SPP), and Number of Sweeps (NS) values were chosen to acquire Hahn echo decay curves (Figure S24 and S25). Both materials display overlapping decay curves under different conditions. The fitted T_m results were summarized in Table S2 and S3. When the SRT values are longer than $5T_1$, they do not affect the T_m. In addition, the Hahn echo decay curves and fitted T_m values are not affected by SPP and NS. These experiments indicate that the spin system can return to the equilibrium between measurements for SRT > $5T_1$. Therefore, we set SRT to be longer than $5T_1$ for T_m characterization.

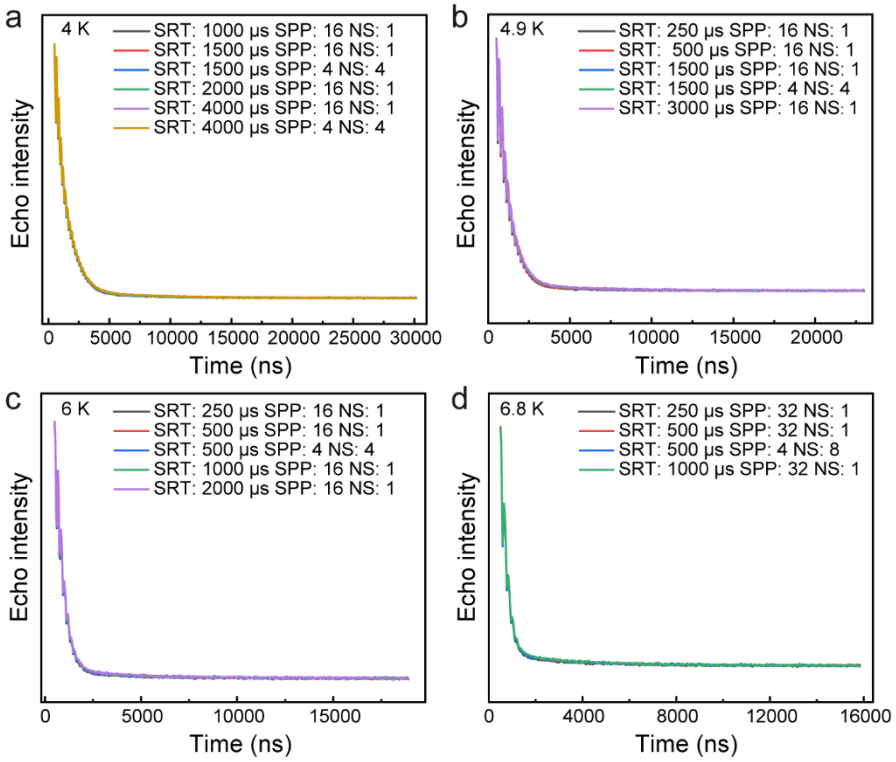

Figure S24. Hahn echo decay curves of **Nd$_1$La$_{99}$** collected using various SRT, SPP and NS at 4 K, 4.9 K, 6 K, and 6.8 K.

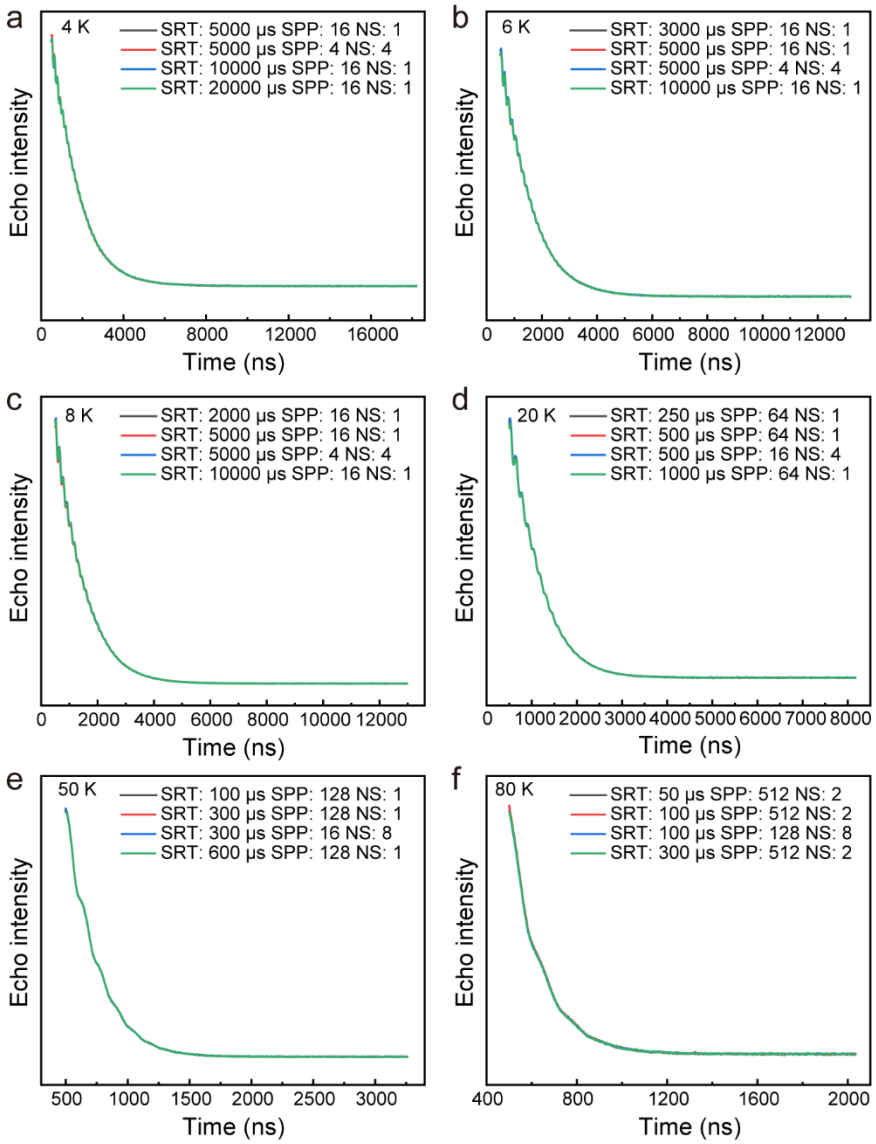

Figure S25. Hahn echo decay curves of $\mathbf{Gd_{0.5}La_{99.5}}$ collected using various SRT, SPP and NS at 4 K, 6 K, 8 K, 20 K, 50 K, and 80 K.

Table S2. T_m for **Nd_1La_{99}** using various SRT, SPP and NS at 4 K, 4.9 K, 6 K, and 6.8 K.

Temperature (K)	Shot Repetition Time (SRT) (μs)	Shots Per Point (SPP)	No. of Sweeps (NS)	T_m (ns)
4	1000 (~ $5T_1$)	16	1	1036
4	1500 (~ $7.5T_1$)	16	1	1045
4	1500 (~ $7.5T_1$)	4	4	1042
4	2000 (~ $10T_1$)	16	1	1053
4	4000 (~ $20T_1$)	16	1	1067
4	4000 (~ $20T_1$)	4	4	1064
4.9	250 (~ $5T_1$)	16	1	764
4.9	500 (~ $10T_1$)	16	1	774
4.9	1500 (~ $30T_1$)	16	1	793
4.9	1500 (~ $30T_1$)	4	4	786
4.9	3000 (~ $60T_1$)	16	1	797
6	250 (~ $16T_1$)	16	1	470
6	500 (~ $33T_1$)	16	1	476
6	500 (~ $33T_1$)	4	4	475
6	1000 (~ $66T_1$)	16	1	482
6	2000 (~ $133T_1$)	16	1	484
6.8	250 (~ $50T_1$)	32	1	309
6.8	500 (~ $100T_1$)	32	1	317
6.8	500 (~ $100T_1$)	4	8	313
6.8	1000 (~ $200T_1$)	32	1	321

Table S3. T_m for **$Gd_{0.5}La_{99.5}$** using various SRT, SPP and NS at 4 K, 6 K, 8 K, 20 K, 50 K, and 80 K.

Temperature (K)	Shot Repetition Time (SRT) (μs)	Shots Per Point (SPP)	No. of Sweeps (NS)	T_m (ns)
4	5000 (~ 5.5T_1)	16	1	1284
4	5000 (~ 5.5T_1)	4	4	1267
4	10000 (~ 11T_1)	16	1	1290
4	20000 (~ 22T_1)	16	1	1284
6	3000 (~ 5T_1)	16	1	1074
6	5000 (~ 8T_1)	16	1	1080
6	5000 (~ 8T_1)	4	4	1072
6	10000 (~ 16T_1)	16	1	1080
8	2000 (~ 5T_1)	16	1	991
8	5000 (~ 13T_1)	16	1	996
8	5000 (~ 13T_1)	4	4	988
8	10000 (~ 26T_1)	16	1	993
20	250 (~ 5T_1)	64	1	666
20	500 (~ 10T_1)	64	1	665
20	500 (~ 10T_1)	16	4	664
20	1000 (~ 20T_1)	64	1	669
50	100 (~ 33T_1)	128	1	247
50	300 (~ 100T_1)	128	1	247
50	300 (~ 100T_1)	16	8	247
50	600 (~ 200T_1)	128	1	248
80	50 (~ 50T_1)	512	2	134
80	100 (~ 100T_1)	512	2	134
80	100 (~ 100T_1)	128	8	133
80	300 (~ 300T_1)	512	2	133

Note S5. Comparison between ESEEM model and mono-exponential decay equation for T_m fitting

Hahn echo decay curves of $\mathbf{Nd_xLa_{100-x}}$ and $\mathbf{Gd_yLa_{100-y}}$ display oscillations stemming from electron spin echo envelope modulation (ESEEM). Accordingly, we tried to use the ESEEM model to fit the T_m:[10]

$$I = A[1 - Bcos(\omega\tau + d)e^{-\frac{\tau}{T_{OSC}}}]e^{-(\frac{2\tau}{T_m})^q} \quad \text{(S19)}$$

where A represents the overall amplitude, B the ESEEM amplitude, ω the ESEEM frequency, T_{OSC} the ESEEM decay time, and q the stretch factor. When the q value is released for fitting, it shows random variations with temperature as shown in Figure S26. This exerts a significant impact on the fitting of T_m and introduces errors. In addition, at high temperatures, the ESEEM oscillatory signals become almost negligible, and the Hahn echo decay curves resemble the mono-exponential decay. Thus, we fixed the q value as 1 for consistency.

As shown in Figure S27−S29, we find that the ESEEM model can fit Hahn echo decay curves collected at relatively low temperature for $\mathbf{Nd_xLa_{100-x}}$. At relatively high temperatures (e.g. above 6.4 K for $\mathbf{Nd_4La_{96}}$), the Hahn echo decay curves cannot be fitted by Equation S19 due to the absence of modulation. The fitting results are summarized in Table S4, which are close to those obtained from mono-exponential decay fitting (Equation S8). Both fitting methods reveal similar temperature dependence of T_m (Figure S30, Table S4 and S6).

We also tried to fit Hahn echo decay curves of $\mathbf{Gd_yLa_{100-y}}$ by the ESEEM model. The ESEEM signals are much weaker than those of $\mathbf{Nd_xLa_{100-x}}$, so the fitting of some data was not good. Nonetheless, the fitting results are essentially consistent with those obtained from mono-exponential decay fitting (Figure S31−S33). Therefore, for consistency, we chose to fit the Hahn echo decay curves of $\mathbf{Nd_xLa_{100-x}}$ and $\mathbf{Gd_yLa_{100-y}}$ by Equation S8.

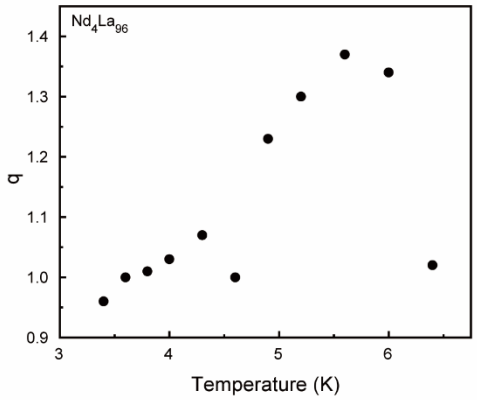

Figure S26. Fitted stretch factors of **Nd_4La_{96}** using the ESEEM model.

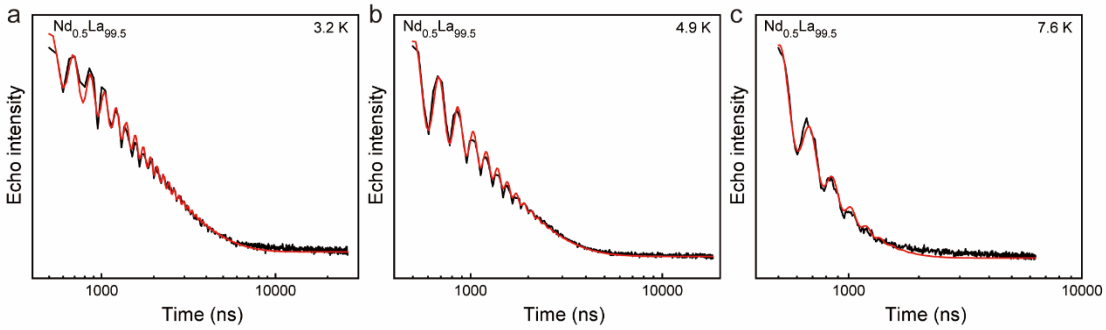

Figure S27. Hahn echo decay curves of **$Nd_{0.5}La_{99.5}$** fitted by Equation S19 at 3.2 K, 4.9 K, and 7.6 K. Red lines are fitting curves.

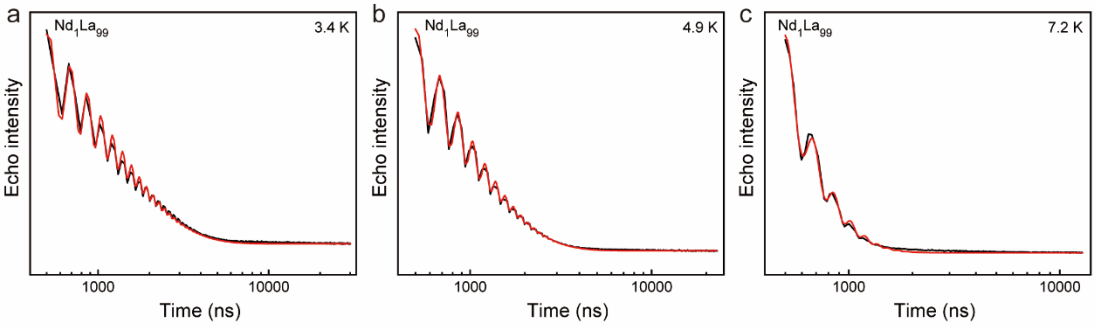

Figure S28. Hahn echo decay curves of **Nd_1La_{99}** fitted by Equation S19 at 3.2 K, 4.9 K, and 7.2 K. Red lines are fitting curves.

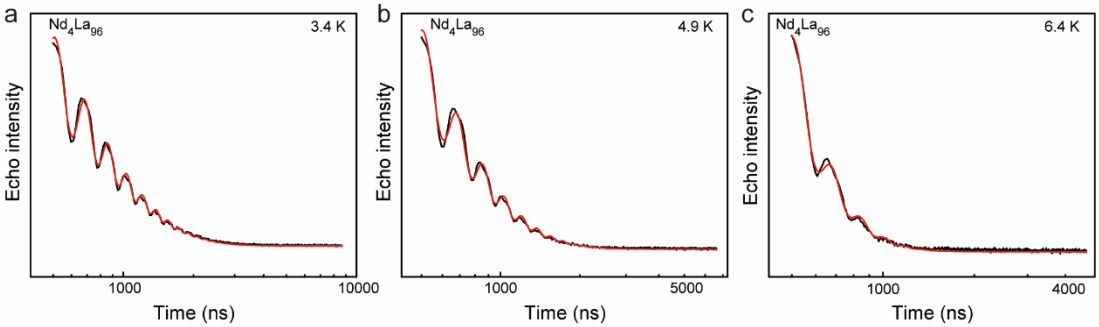

Figure S29. Hahn echo decay curves of **Nd_4La_{96}** fitted by Equation S19 at 3.2 K, 4.9 K, and 6.4 K. Red lines are fitting curves.

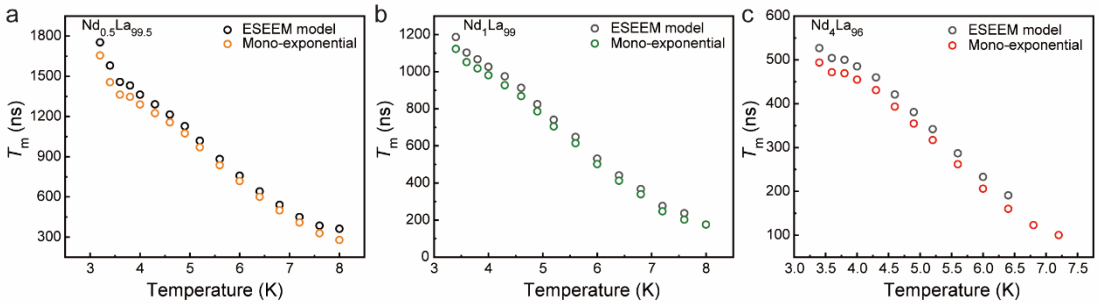

Figure S30. Variable-temperature T_m of **Nd_xLa_{100-x}** fitted by Equation S8 and Equation S19.

Table S4. T_m for **Nd_xLa_{100-x}** (x = 0.5, 1, 4) fitted by Equation S19 at various temperatures from 3.2 K to 8.0 K.

Temperature (K)	**$Nd_{0.5}La_{99.5}$**–T_m (ns)	**Nd_1La_{99}**–T_m (ns)	**Nd_4La_{96}**–T_m (ns)
3.2	1753	–	–
3.4	1580	1187	527
3.6	1458	1103	504
3.8	1432	1067	500
4.0	1363	1026	485
4.3	1291	975	460
4.6	1215	913	421
4.9	1128	825	381
5.2	1019	741	342
5.6	882	648	287
6.0	758	531	233
6.4	641	441	191
6.8	540	367	–
7.2	449	276	–
7.6	385	237	–
8.0	362	–	–

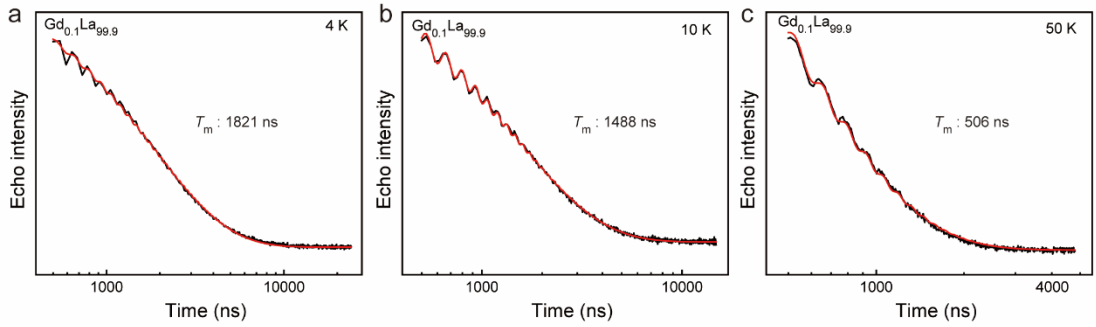

Figure S31. Hahn echo decay curves of **$Gd_{0.1}La_{99.9}$** fitted by Equation S19 at 4 K, 10 K, and 50 K. Red lines are fitting curves.

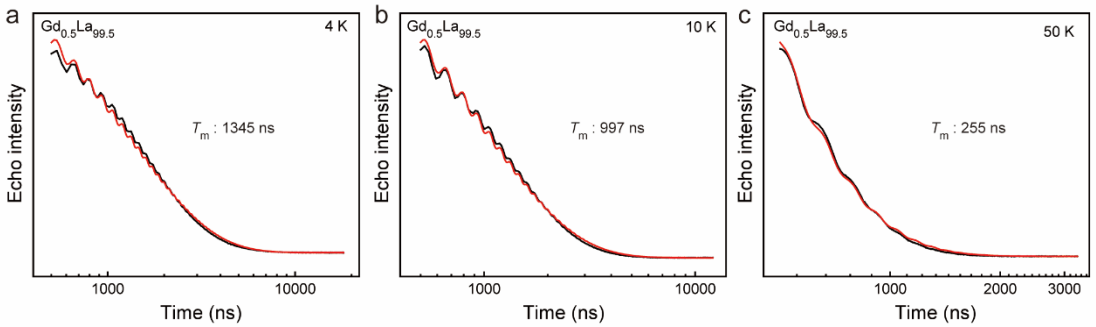

Figure S32. Hahn echo decay curves of **$Gd_{0.5}La_{99.5}$** fitted by Equation S19 at 4 K, 10 K, and 50 K. Red lines are fitting curves.

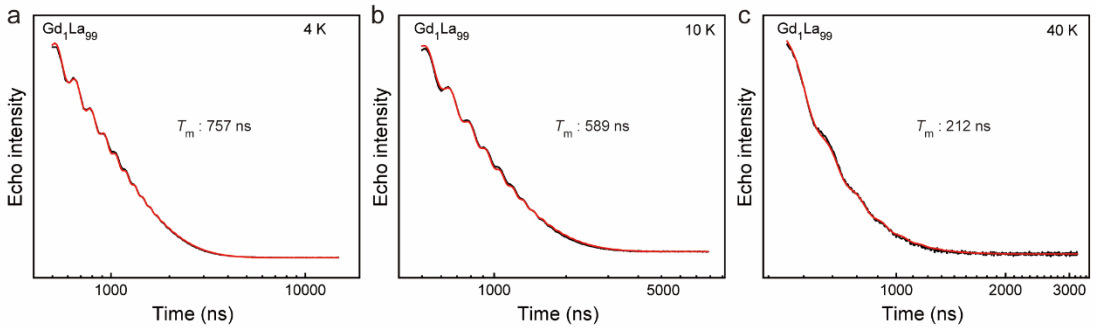

Figure S33. Hahn echo decay curves of **Gd_1La_{99}** fitted by Equation S19 at 4 K, 10 K, and 40 K. Red lines are fitting curves.

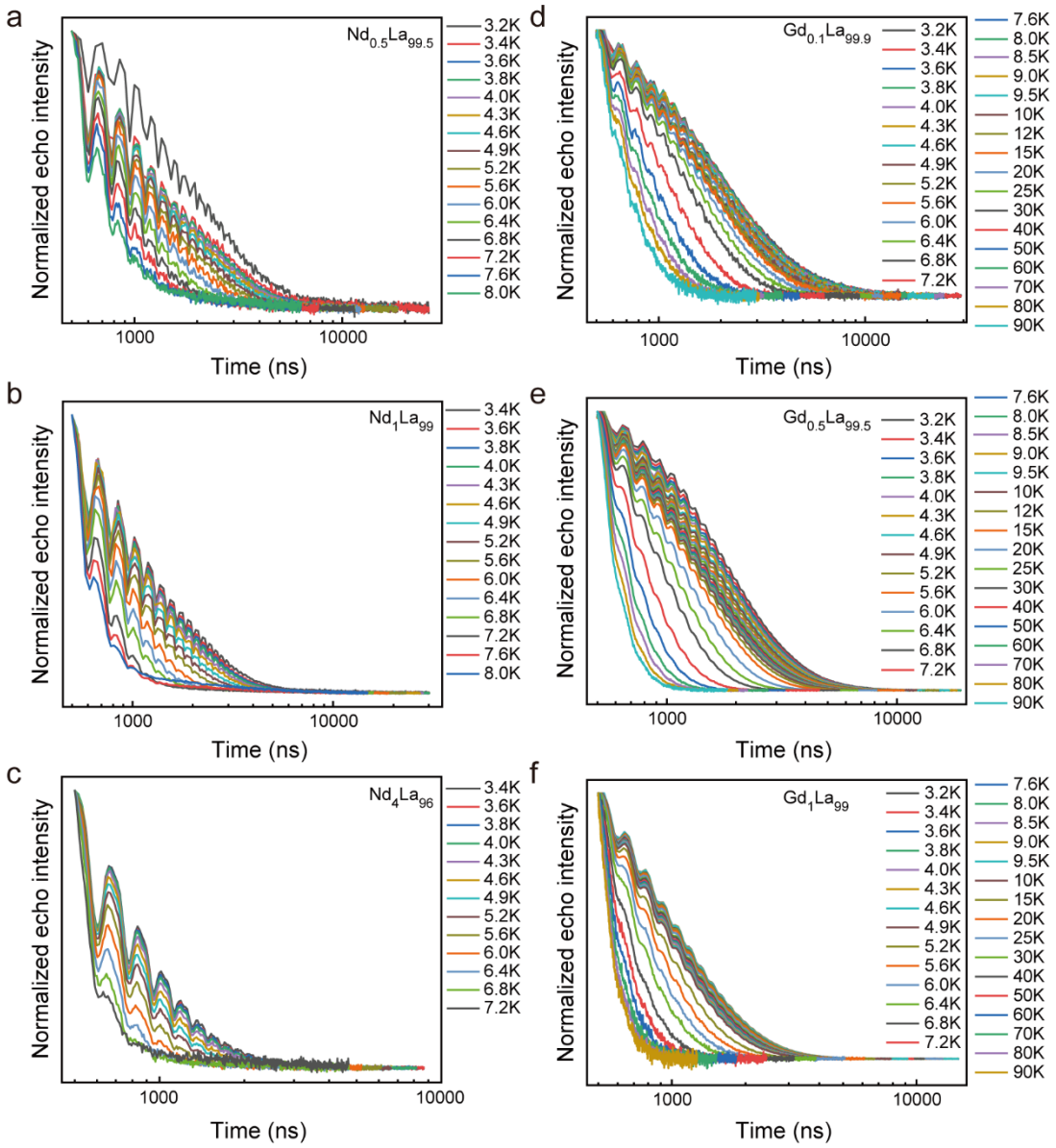

Figure S34. Normalized Hahn echo decay curves of (a) **$Nd_{0.5}La_{99.5}$**, (b) **Nd_1La_{99}**, and (c) **Nd_4La_{96}** collected at various temperatures from 3.2 K to 8.0 K. Normalized Hahn echo decay curves of (d) **$Gd_{0.1}La_{99.9}$**, (e) **$Gd_{0.5}La_{99.5}$**, and (f) **Gd_1La_{99}** collected at various temperatures from 3.2 K to 90 K.

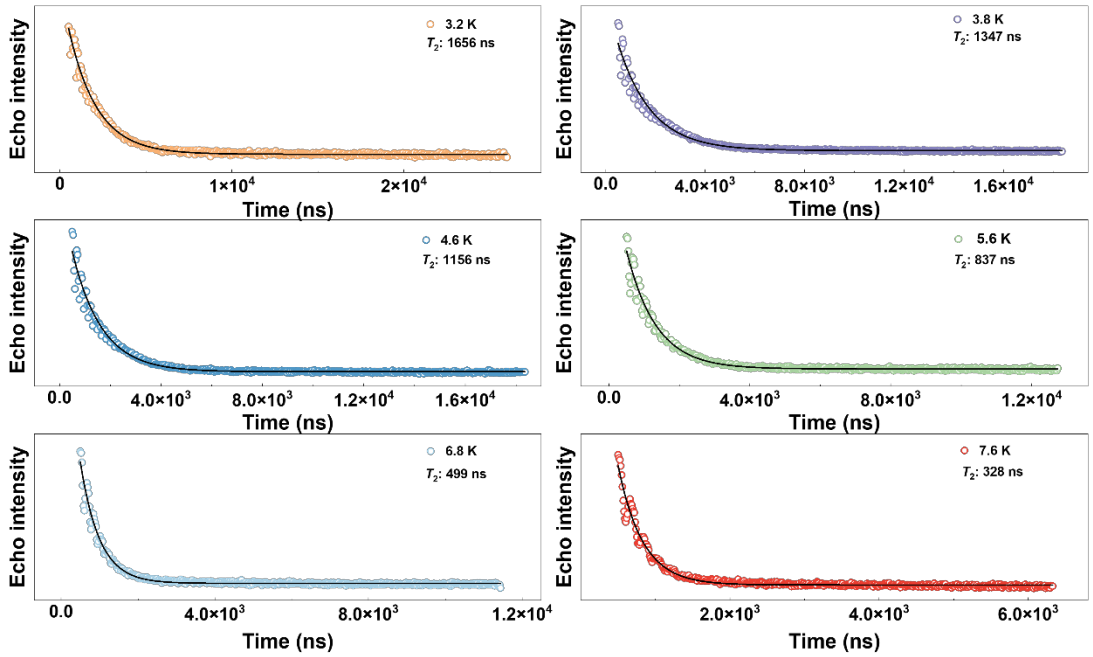

Figure S35. Hahn echo decay curves of $Nd_{0.5}La_{99.5}$ fitted by a mono-exponential decay function (Equation S8) at 3.2 K, 3.8 K, 4.6 K, 5.6 K, 6.8 K, and 7.6 K. Black lines are fitting curves.

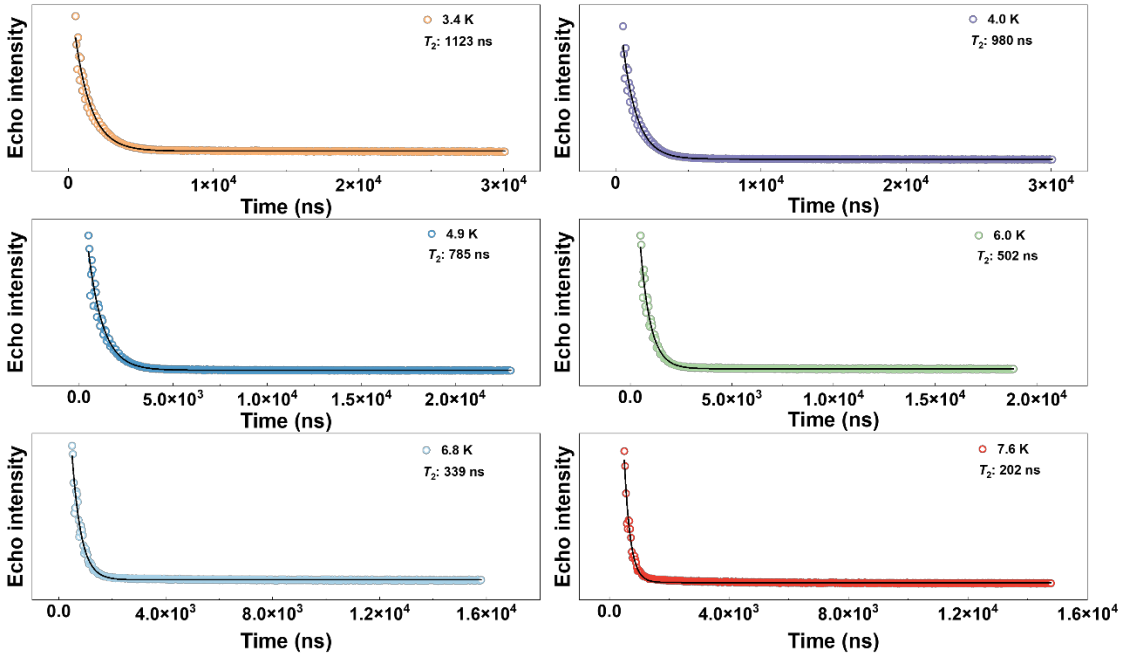

Figure S36. Hahn echo decay curves of Nd_1La_{99} fitted by a mono-exponential decay function (Equation S8) at 3.2 K, 3.8 K, 4.6 K, 5.6 K, 6.8 K, and 7.6 K. Black lines are fitting curves.

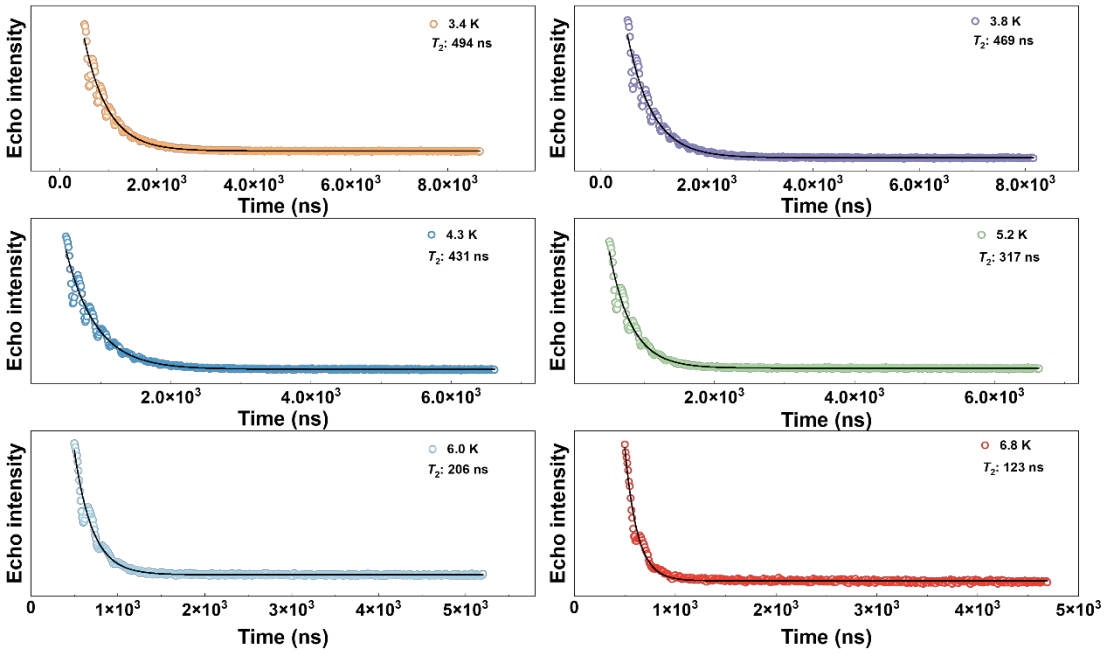

Figure S37. Hahn echo decay curves of **Nd_4La_{96}** fitted by a mono-exponential decay function (Equation S8) at 3.4 K, 3.8 K, 4.3 K, 5.2 K, 6.0 K, and 6.8 K. Black lines are fitting curves.

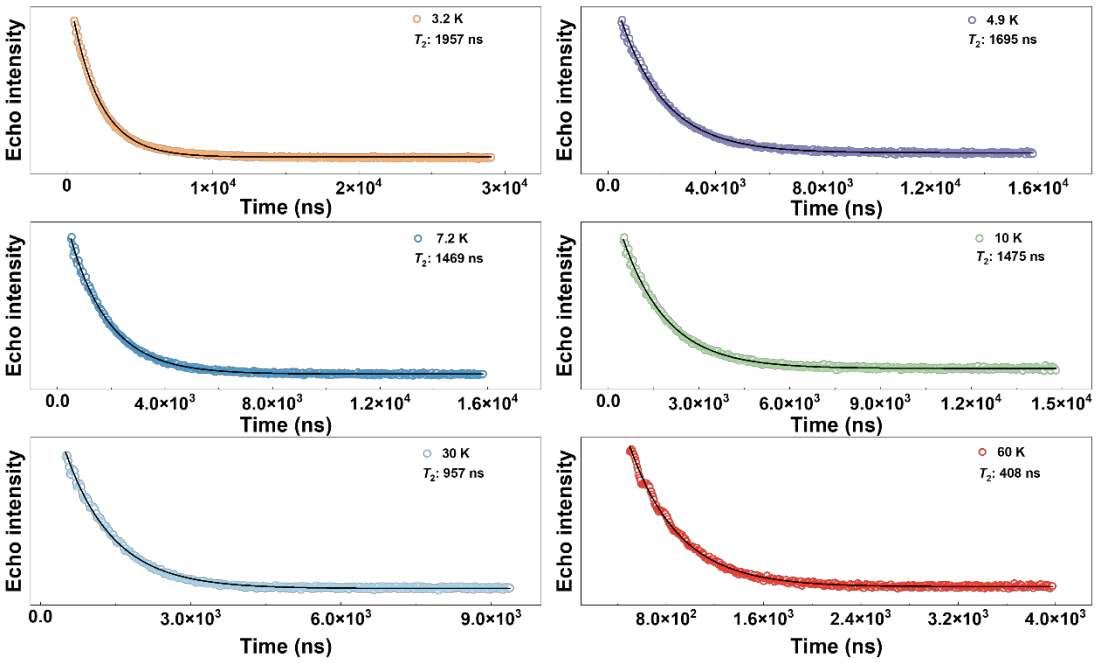

Figure S38. Hahn echo decay curves of **$Gd_{0.1}La_{99.9}$** fitted by a mono-exponential decay function (Equation S8) at 3.2 K, 4.9 K, 7.2 K, 10 K, 30 K, and 60 K. Black lines are fitting curves.

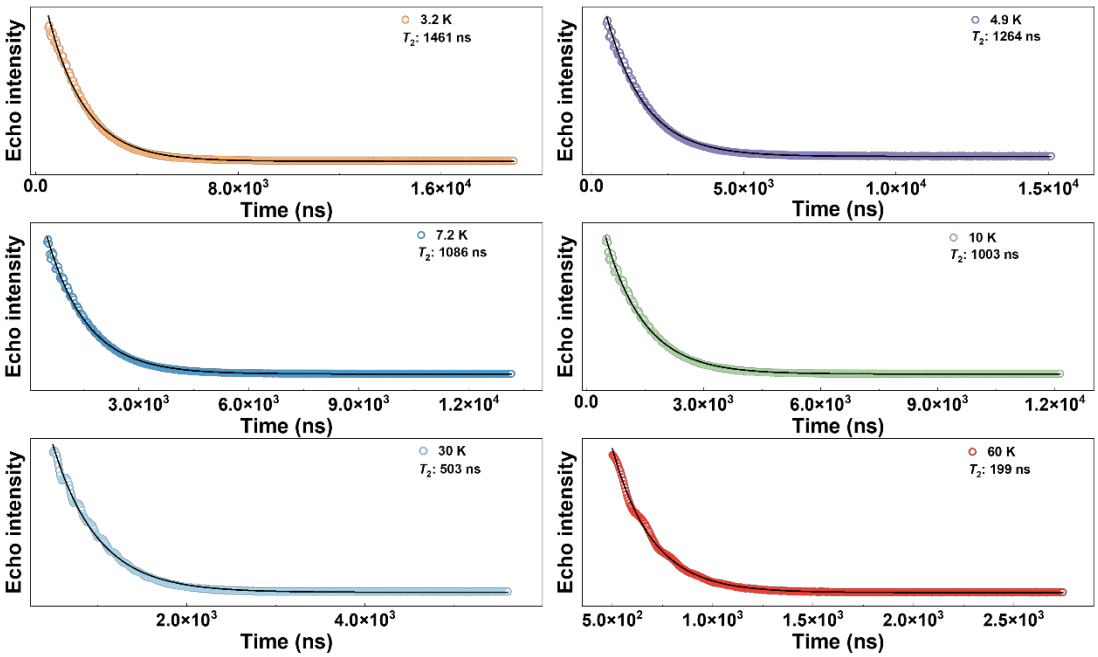

Figure S39. Hahn echo decay curves of **$Gd_{0.5}La_{99.5}$** fitted by a mono-exponential decay function (Equation S8) at 3.2 K, 4.9 K, 7.2 K, 10 K, 30 K, and 60 K. Black lines are fitting curves.

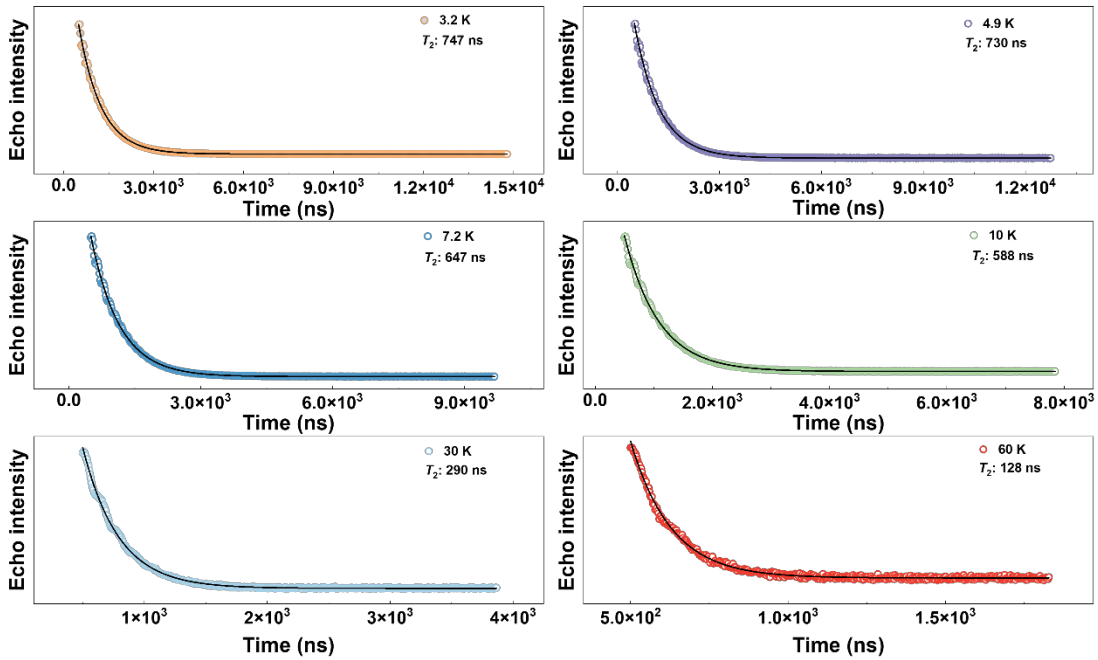

Figure S40. Hahn echo decay curves of **Gd_1La_{99}** fitted by a mono-exponential decay function (Equation S8) at 3.2 K, 4.9 K, 7.2 K, 10 K, 30 K, and 60 K. Black lines are fitting curves.

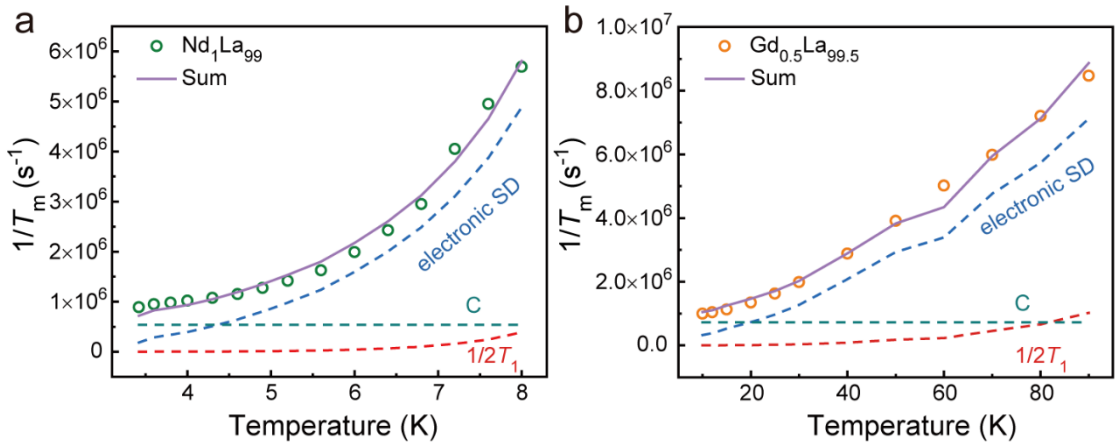

Figure S41. Fitting of $1/T_m$ vs T data for (a) **Nd_1La_{99}** and (b) **$Gd_{0.5}La_{99.5}$** with Equation 5. Red, blue, and green dash lines represent contributions from spin relaxation, electronic SD, and a temperature-independent constant, C, which encompasses contributions from electron spin flip-flop, nuclear SD, and ID. The plum solid line is their sum.

Table S5. Fitting parameters of $1/T_m$ vs T data with Equation 5.

Samples	$A_{SD,e}$ ($s^{-1/2}$)	C (s^{-1})
$Nd_{0.5}La_{99.5}$	3262	487545
Nd_1La_{99}	5539	536880
Nd_4La_{96}	14336	852951
$Gd_{0.1}La_{99.9}$	2057	524474
$Gd_{0.5}La_{99.5}$	4975	721432
Gd_1La_{99}	7248	1488872

Summary of T_1 and T_m

Table S6. T_1 and T_m for $\mathbf{Nd_xLa_{100-x}}$ (x = 0.5, 1, 4) at various temperatures from 3.2 K to 8.0 K.

Temperature (K)	$\mathbf{Nd_{0.5}La_{99.5}}$		$\mathbf{Nd_1La_{99}}$		$\mathbf{Nd_4La_{96}}$	
	T_1 (μs)	T_m (ns)	T_1 (μs)	T_m (ns)	T_1 (μs)	T_m (ns)
3.2	$1.218(5) \times 10^3$	$1.656(16) \times 10^3$	–	–	–	–
3.4	$9.237(32) \times 10^2$	$1.456(20) \times 10^3$	$9.125(14) \times 10^2$	$1.122(14) \times 10^3$	$4.170(15) \times 10^2$	$4.94(7) \times 10^2$
3.6	$3.981(12) \times 10^2$	$1.363\ (18) \times 10^3$	$3.700(7) \times 10^2$	$1.052(13) \times 10^3$	$2.402(7) \times 10^2$	$4.72(7) \times 10^2$
3.8	$2.784(8) \times 10^2$	$1.347(18) \times 10^3$	$2.670(6) \times 10^2$	$1.017(13) \times 10^3$	$1.979(6) \times 10^2$	$4.69(7) \times 10^2$
4.0	$1.995(7) \times 10^2$	$1.290(17) \times 10^3$	$1.954(4) \times 10^2$	$9.80(12) \times 10^2$	$1.500(4) \times 10^2$	$4.55(7) \times 10^2$
4.3	$1.144(3) \times 10^2$	$1.225(16) \times 10^3$	$1.188(3) \times 10^2$	$9.27(13) \times 10^2$	$1.021(3) \times 10^2$	$4.31(6) \times 10^2$
4.6	$7.005(20) \times 10^1$	$1.156(15) \times 10^3$	$7.334(19) \times 10^1$	$8.69(12) \times 10^2$	$6.427(19) \times 10^1$	$3.93(6) \times 10^2$
4.9	$4.587(14) \times 10^1$	$1.074(14) \times 10^3$	$4.762(15) \times 10^1$	$7.85(11) \times 10^2$	$4.270(14) \times 10^1$	$3.55(5) \times 10^2$
5.2	$2.999(10) \times 10^1$	$9.70(13) \times 10^2$	$3.177(10) \times 10^1$	$7.05(10) \times 10^2$	$2.835(10) \times 10^1$	$3.17(5) \times 10^2$
5.6	$1.848(7) \times 10^1$	$8.37(11) \times 10^2$	$1.992(8) \times 10^1$	$6.14(8) \times 10^2$	$1.707(7) \times 10^1$	$2.62(4) \times 10^2$
6.0	$1.144(5) \times 10^1$	$7.18(10) \times 10^2$	$1.204(4) \times 10^1$	$5.02(7) \times 10^2$	$1.048(5) \times 10^1$	$2.06(3) \times 10^2$
6.4	7.420(35)	$6.00(8) \times 10^2$	7.653(27)	$4.12(6) \times 10^2$	6.478(44)	$1.60(2) \times 10^2$
6.8	4.838(32)	$4.99(7) \times 10^2$	4.953(20)	$3.39(5) \times 10^2$	4.330(43)	$1.23(2) \times 10^2$
7.2	3.141(25)	$4.08(6) \times 10^2$	3.184(15)	$2.47(3) \times 10^2$	2.925(39)	$1.00(2) \times 10^2$
7.6	2.159(27)	$3.28(5) \times 10^2$	2.044(10)	$2.02(3) \times 10^2$	–	–
8.0	1.479(28)	$2.79(5) \times 10^2$	1.287(9)	$1.76(3) \times 10^2$	–	–

Table S7. Spin relaxation times (T_1 and T_S), pre-factors (a and b) and T_m for **$Gd_{0.1}La_{99.9}$** at various temperatures from 3.2 K to 90 K.

Temperature (K)	**$Gd_{0.1}La_{99.9}$**					
	a	T_1 (μs)	b	T_S (μs)	b/a	T_m (ns)
3.2	-93(2)	$4.682(71) \times 10^3$	-111(2)	$1.031(25) \times 10^3$	1.19	$1.957(7) \times 10^3$
3.4	-89(2)	$4.021(57) \times 10^3$	-99(2)	$8.69(21) \times 10^2$	1.11	$1.931(7) \times 10^3$
3.6	-86(2)	$3.236(43) \times 10^3$	-87(2)	$6.47(17) \times 10^2$	1.01	$1.897(7) \times 10^3$
3.8	-83(2)	$2.967(41) \times 10^3$	-84(2)	$6.09(16) \times 10^2$	1.01	$1.883(7) \times 10^3$
4.0	-82(1)	$2.628(34) \times 10^3$	-76(1)	$5.29(14) \times 10^2$	0.93	$1.818(6) \times 10^3$
4.3	-70(1)	$2.015(28) \times 10^3$	-70(1)	$4.02(11) \times 10^2$	1.00	$1.778(6) \times 10^3$
4.6	-68(1)	$1.741(24) \times 10^3$	-64(1)	$3.49(10) \times 10^2$	0.94	$1.737(6) \times 10^3$
4.9	-63(1)	$1.543(21) \times 10^3$	-59(1)	$3.23(9) \times 10^2$	0.94	$1.695(6) \times 10^3$
5.2	-65(1)	$1.398(18) \times 10^3$	-54(1)	$2.76(9) \times 10^2$	0.83	$1.659(6) \times 10^3$
5.6	-56(1)	$1.263(18) \times 10^3$	-56(1)	$2.50(7) \times 10^2$	1.00	$1.618(6) \times 10^3$
6.0	-53(1)	$1.044(17) \times 10^3$	-50(1)	$2.29(7) \times 10^2$	0.94	$1.569(6) \times 10^3$
6.4	-53(1)	$8.57(12) \times 10^2$	-44(1)	$1.80(6) \times 10^2$	0.83	$1.520(5) \times 10^3$
6.8	-49(1)	$7.48(12) \times 10^2$	-43(1)	$1.64(6) \times 10^2$	0.88	$1.483(5) \times 10^3$
7.2	-47(1)	$6.39(10) \times 10^2$	-39(1)	$1.40(5) \times 10^2$	0.83	$1.469(5) \times 10^3$
7.6	-43(1)	$5.58(10) \times 10^2$	-38(1)	$1.31(5) \times 10^2$	0.88	$1.462(5) \times 10^3$
8.0	-41(1)	$4.86(8) \times 10^2$	-35(1)	$1.11(4) \times 10^2$	0.85	$1.445(5) \times 10^3$
8.5	-36(1)	$4.19(8) \times 10^2$	-35(1)	$1.04(4) \times 10^2$	0.97	$1.456(6) \times 10^3$

9.0	-35(1)	$3.50(7) \times 10^2$	-32(1)	$8.69(33) \times 10^1$	0.91	$1.465(6) \times 10^3$
9.5	-33(1)	$3.05(6) \times 10^2$	-31(1)	$7.70(28) \times 10^1$	0.94	$1.471(6) \times 10^3$
10	-30.9(8)	$2.58(4) \times 10^2$	-28.6(7)	$6.66(21) \times 10^1$	0.93	$1.475(6) \times 10^3$
12	-78(3)	$1.60(4) \times 10^2$	-80(1)	$4.35(17) \times 10^1$	1.03	$1.465(5) \times 10^3$
15	-58(3)	$8.73(25) \times 10^1$	-65(3)	$2.67(11) \times 10^1$	1.12	$1.415(6) \times 10^3$
20	-44(2)	$3.90(12) \times 10^1$	-46(2)	$1.26(6) \times 10^1$	1.05	$1.280(5) \times 10^3$
25	-32(1)	$2.22(5) \times 10^1$	-37(1)	7.39(22)	1.16	$1.124(5) \times 10^3$
30	-70(4)	$1.43(4) \times 10^1$	-99(4)	4.98(17)	1.41	$9.57(5) \times 10^2$
40	-52(3)	5.77(15)	-55(3)	2.24(9)	1.06	$6.87(3) \times 10^2$
50	-26(3)	3.55(19)	-44(3)	1.41(7)	1.69	$5.10(2) \times 10^2$
60	-66(17)	1.90(19)	-81(15)	0.83(11)	1.23	$4.08(2) \times 10^2$
70	-56(12)	1.26(11)	-53(10）	0.53(9)	0.95	$3.42(2) \times 10^2$
80	–	0.720(8)	–	–	–	$2.94(1) \times 10^2$
90	–	0.562(10)	–	–	–	$2.43(2) \times 10^2$

Table S8. Spin relaxation times (T_1 and T_S), pre-factors (a and b) and T_m for **$Gd_{0.5}La_{99.5}$** at various temperatures from 3.2 K to 90 K.

Temperature (K)	**$Gd_{0.5}La_{99.5}$**					
	a	T_1 (μs)	b	T_S (μs)	b/a	T_m (ns)
3.2	-110(1)	$6.40(5) \times 10^2$	-133(1)	$1.26(2) \times 10^2$	1.21	$1.461(8) \times 10^3$
3.4	-89(1)	$7.85(7) \times 10^2$	-136(1)	$1.42(2) \times 10^2$	1.53	$1.423(7) \times 10^3$
3.6	-76(1)	$8.67(9) \times 10^2$	-133(1)	$1.48(2) \times 10^2$	1.75	$1.396(6) \times 10^3$
3.8	-71(1)	$8.81(10) \times 10^2$	-130(1)	$1.48(2) \times 10^2$	1.83	$1.373(6) \times 10^3$
4.0	-68.6(9)	$8.46(9) \times 10^2$	-122.9(9)	$1.42(2) \times 10^2$	1.79	$1.351(6) \times 10^3$
4.3	-63.7(9)	$7.78(9) \times 10^2$	-114.0(9)	$1.36(2) \times 10^2$	1.79	$1.324(6) \times 10^3$
4.6	-57.8(8)	$7.25(9) \times 10^2$	-107.9(8)	$1.29(2) \times 10^2$	1.87	$1.286(5) \times 10^3$
4.9	-52.5(8)	$7.01(9) \times 10^2$	-101.7(8)	$1.27(2) \times 10^2$	1.94	$1.264(6) \times 10^3$
5.2	-48.4(8)	$6.54(8) \times 10^2$	-93.8(8)	$1.20(2) \times 10^2$	1.94	$1.228(5) \times 10^3$
5.6	-41.9(7)	$5.97(8) \times 10^2$	-84.7(7)	$1.14(2) \times 10^2$	2.02	$1.190(5) \times 10^3$
6.0	-38.2(7)	$5.53(8) \times 10^2$	-77.6(7)	$1.07(2) \times 10^2$	2.03	$1.168(5) \times 10^3$
6.4	-33.7(6)	$5.15(7) \times 10^2$	-70.9(6)	$1.02(1) \times 10^2$	2.10	$1.138(5) \times 10^3$
6.8	-30.0(6)	$4.82(7) \times 10^2$	-65.2(6)	$9.67(13) \times 10^1$	2.17	$1.110(5) \times 10^3$
7.2	-26.8(6)	$4.40(7) \times 10^2$	-60.7(6)	$9.07(12) \times 10^1$	2.26	$1.086(4) \times 10^3$
7.6	-23.6(6)	$4.16(7) \times 10^2$	-56.6(5)	$8.65(12) \times 10^1$	2.40	$1.067(4) \times 10^3$
8.0	-22.7(6)	$3.50(6) \times 10^2$	-52.2(5)	$7.87(11) \times 10^1$	2.30	$1.053(4) \times 10^3$
8.5	-20.9(5)	$3.17(5) \times 10^2$	-47.7(5)	$7.36(10) \times 10^1$	2.28	$1.037(4) \times 10^3$

9.0	-18.5(5)	$2.91(5) \times 10^{2}$	-45.3(5)	$6.84(9) \times 10^{1}$	2.45	$1.024(4) \times 10^{3}$
9.5	-16.5(5)	$2.63(5) \times 10^{2}$	-42.9(5)	$6.33(9) \times 10^{1}$	2.60	$1.015(4) \times 10^{3}$
10	-48(1)	$2.38(5) \times 10^{2}$	-126(1)	$5.79(8) \times 10^{1}$	2.63	$1.003(4) \times 10^{3}$
12	-33(1)	$1.71(4) \times 10^{2}$	-102(1)	$4.31(6) \times 10^{1}$	3.09	$9.58(4) \times 10^{2}$
15	-26.6(8)	$8.87(16) \times 10^{1}$	-66.8(8)	$2.61(3) \times 10^{1}$	2.51	$8.84(4) \times 10^{2}$
20	-40(2)	$4.63(11) \times 10^{1}$	-109(2)	$1.39(2) \times 10^{1}$	2.73	$7.44(4) \times 10^{2}$
25	-19(1)	$2.64(8) \times 10^{1}$	-53(1)	8.50(15)	2.79	$6.14(3) \times 10^{2}$
30	-9.5(7)	$1.54(6) \times 10^{1}$	-23.4(7)	5.45(12)	2.46	$5.03(3) \times 10^{2}$
40	-6.9(8)	5.73(29)	-8.1(7)	2.25(15)	1.17	$3.47(2) \times 10^{2}$
50	-24.7(8)	2.87(4)	-26.6(8)	1.09(3)	1.08	$2.56(1) \times 10^{2}$
60	-36(3)	2.16(8)	-284(2)	0.685(7)	7.89	$1.991(7) \times 10^{2}$
70	-130(4)	1.09(2)	-92(3)	0.373(22)	0.71	$1.672(6) \times 10^{2}$
80	-84(2)	0.752(9)	-98(20)	0.173(19)	1.17	$1.389(5) \times 10^{2}$
90	–	0.488(4)	–	–	–	$1.181(4) \times 10^{2}$

Table S9. Spin relaxation times (T_1 and T_S), pre-factors (a and b) and T_m for **Gd_1La_{99}** at various temperatures from 3.2 K to 90 K.

Temperature (K)	**Gd_1La_{99}**					
	a	T_1 (μs)	b	T_S (μs)	b/a	T_m (ns)
3.2	-50.1(5)	$1.41(1) \times 10^2$	-59.9(5)	$2.67(3) \times 10^1$	1.20	$7.47(2) \times 10^2$
3.4	-45.2(4)	$1.54(1) \times 10^2$	-58.1(4)	$2.79(4) \times 10^1$	1.29	$7.52(2) \times 10^2$
3.6	-39.5(4)	$1.76(2) \times 10^2$	-55.8(4)	$2.99(4) \times 10^1$	1.41	$7.54(2) \times 10^2$
3.8	-38.1(4)	$1.82(2) \times 10^2$	-55.1(4)	$3.04(4) \times 10^1$	1.45	$753(2) \times 10^2$
4.0	-36.0(4)	$1.89(2) \times 10^2$	-53.9(4)	$3.08(4) \times 10^1$	1.50	$7.52(2) \times 10^2$
4.3	-32.6(4)	$2.00(2) \times 10^2$	-51.7(4)	$3.14(4) \times 10^1$	1.59	$7.49(2) \times 10^2$
4.6	-29.5(3)	$2.09(2) \times 10^2$	-50.0(4)	$3.24(4) \times 10^1$	1.69	$742(2) \times 10^2$
4.9	-27.2(3)	$2.13(2) \times 10^2$	-48.4(4)	$3.23(5) \times 10^1$	1.78	$7.30(2) \times 10^2$
5.2	-25.6(3)	$2.04(2) \times 10^2$	-46.0(4)	$3.15(5) \times 10^1$	1.80	$7.22(2) \times 10^2$
5.6	-23.2(3)	$2.01(3) \times 10^2$	-42.9(4)	$3.11(5) \times 10^1$	1.85	$7.08(2) \times 10^2$
6.0	-21.5(3)	$1.93(2) \times 10^2$	-40.6(3)	$2.99(4) \times 10^1$	1.89	$6.92(2) \times 10^2$
6.4	-19.3(3)	$1.88(3) \times 10^2$	-38.4(3)	$2.93(4) \times 10^1$	1.99	$6.74(2) \times 10^2$
6.8	-17.8(3)	$1.78(3) \times 10^2$	-36.0(3)	$2.81(4) \times 10^1$	2.02	$6.62(2) \times 10^2$
7.2	-16.9(3)	$1.64(2) \times 10^2$	-33.5(3)	$2.67(4) \times 10^1$	1.98	$6.47(2) \times 10^2$
7.6	-15.3(3)	$1.60(3) \times 10^2$	-32.0(3)	$2.60(4) \times 10^1$	2.09	$6.36(2) \times 10^2$
8.0	-14.2(3)	$1.53(3) \times 10^2$	-30.4(3)	$2.53(4) \times 10^1$	2.14	$6.27(2) \times 10^2$
8.5	-12.8(3)	$1.41(3) \times 10^2$	-28.3(3)	$2.42(4) \times 10^1$	2.21	$6.17(2) \times 10^2$

9.0	-12.3(3)	$1.27(2) \times 10^{2}$	-26.1(3)	$2.23(4) \times 10^{1}$	2.12	$6.04(2) \times 10^{2}$
9.5	-12.3(2)	$1.10(2) \times 10^{2}$	-24.1(2)	$2.00(3) \times 10^{1}$	1.96	$5.96(2) \times 10^{2}$
10	-12.2(2)	$9.78(15) \times 10^{1}$	-22.1(2)	$1.78(3) \times 10^{1}$	1.81	$5.88(2) \times 10^{2}$
12	–	–	–	–	–	–
15	-6.0(2)	$5.49(10) \times 10^{1}$	-15.2(2)	$1.16(2) \times 10^{1}$	2.53	$5.00(2) \times 10^{2}$
20	-3.3(1)	$3.60(9) \times 10^{1}$	-11.3(1)	7.58(11)	3.42	$4.20(2) \times 10^{2}$
25	-2.17(8)	$2.19(6) \times 10^{1}$	-8.06(8)	5.22(7)	3.71	$3.48(1) \times 10^{2}$
30	-1.33(8)	$1.47(5) \times 10^{1}$	-6.01(7)	3.82(6)	4.52	$2.90(1) \times 10^{2}$
40	-0.81(9)	6.05(34)	-2.72(8)	2.02(6)	3.36	$2.10(1) \times 10^{2}$
50	-0.39(6)	3.33(23)	-1.30(5)	1.23(4)	3.33	$1.61(1) \times 10^{2}$
60	-0.18(6)	2.01(27)	-0.58(5)	0.84(5)	3.22	$1.28(1) \times 10^{2}$
70	-0.14(5)	1.17(13)	-0.22(4)	0.52(7)	1.57	$1.057(6) \times 10^{2}$
80	-11(2)	0.699(58)	-5(1)	0.28(15)	0.45	$9.23(4) \times 10^{1}$
90	–	0.468(15)	–	–	–	$8.31(6) \times 10^{1}$

References

(1) C. Hua, H. M. Tay, Q. He and T. D. Harris, A series of early lanthanide chloranilate frameworks with a square grid topology, *Aust. J. Chem.*, 2019, **72**, 778−785.

(2) S. Stoll and A. Schweiger, EasySpin, a comprehensive software package for spectral simulation and analysis in EPR, *J. Magn. Reson.*, 2006, **178**, 42−55.

(3) P. L. Feng, C. C. Beedle, C. Koo, J. Lawrence, S. Hill and D. N. Hendrickson, Origin of magnetization tunneling in single-molecule magnets as determined by single-crystal high-frequency EPR, *Inorg. Chim. Acta*, 2008, **361**, 3465−3480.

(4) J. Wang, Y. Jing, M. H. Cui, Y. M. Lu, Z. Ouyang, C. Shao, Z. Wang and Y. Song, Spin qubit in a 2D $Gd^{III}Na^{I}$-based oxamato supramolecular coordination framework, *Chem. Eur. J.*, 2023, **29**, e202301771.

(5) L. Sun, L. Yang, J.-H. Dou, J. Li, G. Skorupskii, M. Mardini, K. O. Tan, T. Chen, C. Sun, J. J. Oppenheim, R. G. Griffin, M. Dincă and T. Rajh, Room-temperature quantitative quantum sensing of lithium ions with a radical-embedded metal–organic framework, *J. Am. Chem. Soc.*, 2022, **144**, 19008−19016.

(6) S. Hartmann and E. Hahn, Nuclear double resonance in the rotating frame, *Phys. Rev.*, 1962, **128**, 2042−2053.

(7) S. Takahashi, J. van Tol, C. C. Beedle, D. N. Hendrickson, L.-C. Brunel and M. S. Sherwin, Coherent manipulation and decoherence of S=10 single-molecule magnets, *Phys. Rev. Lett.*, 2009, **102**, 087603.

(8) C. B. Wilson, M. Qi, S. Han and M. S. Sherwin, Gadolinium spin decoherence mechanisms at high magnetic fields, *J. Phys. Chem. Lett.*, 2023, **14**, 10578−10584.

(9) C. E. Jackson, T. Ngendahimana, C.-Y. Lin, G. R. Eaton, S. S. Eaton, and J. M. Zadrozny, Impact of counter ion methyl groups on spin relaxation in $[V(C_6H_4O_2)_3]^{2-}$. *J. Phys. Chem. C*, 2022, **126**, 7169−7176.

(10) A. K. Oanta, K. A. Collins, A. M. Evans, S. M. Pratik, L. A. Hall, M. J.

Strauss, S. R. Marder, D. M. D'Alessandro, T. Rajh, D. E. Freedman, H. Li, J.-L. Brédas, L. Sun, and W. R. Dichtel, Electronic spin qubit candidates arrayed within layered two-dimensional polymers, *J. Am. Chem. Soc.*, 2022, **145**, 689−696.